Geophysical Journal International

Geophys. J. Int. (2012) **191,** 1049–1066 doi: 10.1111/j.1365-246X.2012.05617.x

Modelling of the total electronic content and magnetic field anomalies generated by the 2011 Tohoku-Oki tsunami and associated acoustic-gravity waves

E. A. Kherani,[1] P. Lognonné,[1] H. Hébert,[2] L. Rolland,[3] E. Astafyeva,[1] G. Occhipinti,[1] P. Coïsson,[1] D. Walwer[1] and E. R. de Paula[4]

[1] *Institut de Physique du Globe de Paris, Sorbonne Paris Cité, Univ Paris Diderot,* F-75005 *Paris, France. E-mail: alam@dae.inpe.br*
[2] *CEA, DAM, DIF,* F-91297 *Arpajon, France*
[3] *Géoazur, Observatoire de La Côte d'Azur, IRD, CNRS:* UMR7329, *Universite de Nice Sophia, INSU* 250 *av. A. Einstein,* 06560 *Valbonne, France*
[4] *Instituto Nacional de Pesquisas Espaciais, São José dos Campos,* 1222 7010, *Brazil*

Accepted 2012 July 19. Received 2012 July 19; in original form 2011 November 28

SUMMARY

In this work, numerical simulations of the atmospheric and ionospheric anomalies are performed for the Tohoku-Oki tsunami (2011 March 11). The Tsunami–Atmosphere–Ionosphere (TAI) coupling mechanism via acoustic gravity waves (AGWs) is explored theoretically using the TAI-coupled model. For the modelled tsunami wave as an input, the coupled model simulates the wind, density and temperature disturbances or anomalies in the atmosphere and electron density/magnetic anomalies in the F region of the ionosphere. Also presented are the GPS-total electron content (TEC) and ground-based magnetometer measurements during the first hour of tsunami and good agreements are found between modelled and observed anomalies. At first, within 6 min from the tsunami origin, the simulated wind anomaly at 250 km altitude and TEC anomaly appear as the dipole-shaped disturbances around the epicentre, then as the concentric circular wave fronts radially moving away from the epicentre with the horizontal velocity ∼800 m s^{-1} after 12 min followed by the slow moving (horizontal velocity ∼250 m s^{-1}) wave disturbance after 30 min. The detailed vertical–horizontal propagation characteristics suggest that the anomalies appear before and after 30 min are associated with the acoustic and gravity waves, respectively. Similar propagation characteristics are found from the GPS-TEC and magnetic measurements presented here and also reported from recent studies. The modelled magnetic anomaly in the F region ionosphere is found to have similar temporal variations with respect to the epicentre distance as that of the magnetic anomaly registered from the ground-based magnetometers. The high-frequency component ∼10 min of the simulated wind, TEC and magnetic anomalies in the F region develops within 6–7 min after the initiation of the tsunami, suggesting the importance of monitoring the high-frequency atmospheric/ionospheric anomalies for the early warning. These anomalies are found to maximize across the epicentre in the direction opposite to the tsunami propagation suggesting that the large atmospheric/ionospheric disturbances are excited in the region where tsunami does not travel.

Key words: Acoustic-gravity waves; Ionosphere/atmosphere interactions; Tsunamis.

1 INTRODUCTION

The magnitude 9.0 Tohoku-Oki earthquake occurred at 05:46:23 UT off the east coast of Honshu, Japan (38.322N, 142.369E). Waves generated in the solid Earth, ocean, atmosphere and ionosphere were detected by acceleration, displacement and pressure sensors on the Earth surface and ocean bottom (e.g. Maeda *et al.* 2011; Nishimura *et al.* 2011; Simon *et al.* 2011) and also by various ionospheric sensors such as GPS dual frequency sensor and all-sky imagers monitoring the anomalies in the ionosphere (Heki 2011; Makela *et al.* 2011; Maruyama *et al.* 2011; Rolland *et al.* 2011a). Following the pioneering observations of Calais & Minster (1995) and Artru *et al.* (2005) for seismic and tsunamigenic signals, these ionospheric anomalies are interpreted on the basis of the dynamic coupling of the solid/ocean with the atmospheric and ionospheric systems [See Lognonné *et al.* (1998), Lognonné (2009) and Watada & Kanamori (2010) for the interior/atmospheric seismic coupling; Artru *et al.* (2004, 2005), Occhipinti *et al.* (2006, 2008) and Hickey *et al.* (2009) for the tsunami waves; Kherani *et al.* (2009) for the acoustic–ionospheric waves coupling;

Dautermann *et al.* (2009) for the volcanic triggered acoustic waves]. According to this coupling mechanism, the surface/sea level vertical displacement during earthquake leads to the excitation of acoustic gravity wave (AGW) in the atmosphere. These waves excite the wind disturbances in the atmosphere (referred as coseismic atmospheric disturbances or CADs) and TEC disturbances in the ionosphere (referred as coseismic ionospheric disturbances or CIDs).

For the Sumatra tsunami, the modelling study by Occhipinti *et al.* (2006) finds good agreement between modelled and observed CIDS. Modelling studies by Hickey *et al.* (2010) have suggested that appreciable modulations in the 630.0 nm air-glow intensity should be caused by tsunami-driven AGWs. This simulation prediction was recently confirmed by Makela *et al.* (2011) for the first time, by observing air-glow disturbances in the all-sky image photometer during Tohoku-Oki tsunami.

For the Tohoku-Oki tsunami, number of studies have reported the various aspects of CIDs observed from the GPS-TEC measurements (Astafyeva *et al.* 2011; Chen *et al.* 2011; Heki 2011; Liu *et al.* 2011; Rolland *et al.* 2011b; Tsugawa *et al.* 2011): CIDs with velocity $\sim$1.5–3.5 km s^{-1} observed within 7 min (30 min) after the tsunami initiation related to the seismic waves, including near-field body waves and remote Rayleigh and tsunami wave. Also observed are the CIDs of intermediate velocity $\sim$1 km s^{-1}–600 m s^{-1} 10 min after the tsunami initiation (Liu *et al.* 2011; Rolland *et al.* 2011b) and they are associated with the acoustic waves as shown by Rolland *et al.* (2011b) using normal mode analysis. Mastumara *et al.* (2011) have carried out the simulation of atmospheric waves from the impulsive source and found the good agreement between modelled CADs and observed CIDs during Tohoku-Oki tsunami. Occhipinti *et al.* (2011) have carried out the simulation of atmospheric gravity waves excited by the simulated tsunami wavefield for the Tohoku-Oki tsunami that travels as far as Hawaii and found very good agreement with airglow observation (Makela *et al.* 2011) over Hawaii.

Utada *et al.* (2011) have reported the detailed magnetometer measurements during Tohoku-Oki tsunami and identified the magnetic anomaly associated with the tsunami based on temporal variations of the measured field with the epicentre distance. These variations measured from 16 stations, clearly show the sharp impulsive magnetic anomaly near the epicentre and tends to broaden with distance suggesting that they are associated with the tsunami. Moreover, the correlation of decreasing features of D (westward) and Z (upward) suggests that this phenomenon is caused by the ionospheric disturbance. Based on the dynamo theory, they have also presented the theoretical estimation of the *Z*-component triggered by the tsunami-induced ocean current and fairly good agreement is found with the observation.

Aforementioned GPS-TEC [see e.g. Lognonné *et al.* (2006) for data processing methodology] and magnetic field measurements provide detailed dynamics of ionospheric anomalies during the Tohoku-Oki tsunami. These detailed temporal/spatial characteristics of anomalies including various type of wave characteristics motivate us to carry out, in this study, the simulation of CIDs and magnetic anomaly excited during Tohoku-Oki tsunami for which the simulation studies so far remained focus on the simulation of CADs. Moreover, to have realistic comparison between simulation and observation, realistic tsunami of Tohoku-Oki with the tsunami modelling technique of Hébert *et al.* (2006; for detail, Occhipinti *et al.* 2011) will be used. Together with the simulation, GPS-TEC observations and magnetometer measurements from GSI networks during the Tohoku-Oki tsunami are also presented.

2 TSUNAMI–ATMOSPHERE–IONOSPHERE (TAI)-COUPLED SIMULATION MODEL

The TAI coupling mechanism is accomplished in three steps: (i) the excitation of tsunami wave during the Tohoku-Oki tsunami, (ii) the excitation of AGWs by the tsunami wave and (iii) the excitation of ionospheric anomalies by AGWs. The tsunami wave modelling is performed following the method described by Hébert *et al.* (2006), by using the preliminary source of USGS for Tohoku-Oki tsunami (provided at http://earthquake.usgs.gov/earthquakes) and is used as an input in the present model. The second and third steps of the coupling are accomplished using the non-linear 3-D computational modelling that includes modelling of tsunami triggered AGWs in the atmosphere using the non-hydrostatic-viscous wave equation (Kherani *et al.* 2011) and modelling of hydro-magnetic fluctuations in the ionosphere using hydro-magnetic equations (Kherani *et al.* 2009).

Kherani *et al.* (2011) have derived the wave equation of AGWs using Navier–Stokes equations namely the continuity, momentum and energy equations in the atmosphere. We start from the Navier–Stokes equation (e.g. Landau & Lifchitz 1987) and assume that the space variations of the viscosity are small compared to the wavelength of the gravity waves, which lead to

$$\frac{\partial \vec{W}'}{\partial t} + \vec{W}' \cdot \nabla \vec{W}' = -\frac{1}{\rho}\nabla p + \vec{g} + \frac{1}{\rho}\left(\mu \nabla^2 \vec{W}' + \left(\zeta + \frac{\mu}{3}\right)\nabla\left(\nabla \cdot \vec{W}'\right)\right); \quad \vec{W}' = \vec{W} + \vec{W}_o, \quad (1)$$

$$\frac{\partial \rho}{\partial t} + \nabla \cdot \left(\rho \vec{W}'\right) = 0; \quad (2)$$

$$\frac{\partial p}{\partial t} + \left(\vec{W}' \cdot \nabla\right) p + \gamma p \nabla \cdot \vec{W}' = 0, \quad (3)$$

where $\vec{W}$ is the perturbation wind, W_o is the background wind derived from the horizontal wind model (HWM) model, $p = \frac{R\rho T}{\mathcal{M}_{\rm m}}$ is the pressure, (ρ, T) are the atmospheric mass density and temperature, while μ and ζ are the dynamic first and second viscosity and R and $\mathcal{M}_{\rm m}$ are the perfect gas constant and molar mass, respectively. No assumption of linearity is made in writing $\vec{W}' = \vec{W} + \vec{W}_o$ and the perturbation wind $\vec{W}$ may become of the same order as the mean background wind $\vec{W}_o$, that is, the above equations keep non-linearity in $\vec{W}$. By taking the time derivative of the momentum equation for the wind $\vec{W}'$, and again substituting time derivatives of the density (ρ), wind ($\vec{W}'$) and pressure (p) from the Navier–Stokes equations, the wave equation for the wind $\vec{W}'$ of AGWs is obtained in the following form:

$$\frac{\partial^2 \vec{W}'}{\partial t^2} = \frac{1}{\rho}\nabla\left(\gamma p \nabla \cdot \vec{W}'\right) - \frac{\nabla p}{\rho}\nabla \cdot \left(\rho \vec{W}'\right) + \frac{1}{\rho}\nabla\left(\vec{W}' \cdot \nabla\right) p + \frac{\partial}{\partial t}\left(\nu \nabla^2 \vec{W}' + \left(\zeta' + \frac{\nu}{3}\right)\nabla\left(\nabla \cdot \vec{W}'\right)\right) - \frac{\partial}{\partial t}\left(\vec{W}' \cdot \nabla \vec{W}'\right). \quad (4)$$

Here $\nu = \mu/\rho$ and $\zeta' = \zeta/\rho$ are the first and second kinematic viscosities. The first four terms in the above equation correspond to the non-dispersive AGW and leads to the dispersion relation for the AGWs under normal-mode analysis as shown in Appendix A. The last two terms are associated with the dynamic viscosity coefficient or friction force and the inertial force, respectively. ζ' represents the ratio of second viscosity coefficient to kinematic viscosity coefficient and its relative ratio as compared to the first viscosity

coefficient is taken equals to 0.6 (de Groot *et al.* 2011). Note however that we neglect the non-adiabatic effects in our approach as well as collision effects with ions, which might generate additional source of attenuation (Hickey *et al.* 2009).

The derived wave eq. (4) here has the identical acoustic and gravity terms as the wave equation derived by Kherani *et al.* (2011). The dissipative viscous terms were approximated in the derivation of Kherani *et al.* (2011) while complete dissipative viscous term is considered here in the wave eq. (4). Also, the inertial force term is the newly added term in (4) and was neglected in the derivation of Kherani *et al.* (2011). In Appendices A and B, the dispersion relation of AGWs is derived using eq. (4) without and with the dissipative term, respectively. These dispersion relations are found to be identical to the corresponding known dispersion relations derived in the literature.

The hydromagnetic equations in the ionosphere are written as follows (Kherani *et al.* 2009):

$$\frac{\partial \vec{u}_s}{\partial t} = \frac{q_s}{m_s}(\vec{E} + \vec{u}_s \times \vec{B}_o) - \nu_s \vec{u}_s + \nu_s \vec{W}' \,, \tag{5}$$

$$\frac{\partial n_s}{\partial t} + \nabla \cdot (n_s \vec{u_s}) = P - L \,, \tag{6}$$

$$\nabla^2 \vec{E} - \nabla(\nabla \cdot \vec{E}) - \frac{1}{c^2}\frac{\partial^2 \vec{E}}{\partial t^2} - \mu_o \frac{\partial \vec{J}}{\partial t} = 0 \,, \tag{7}$$

$$\vec{J} = \underline{\sigma} \cdot \vec{E} + \vec{J}_w; \quad \vec{J}_w = e(n_i \vec{u}_i - n_e \vec{u}_e) \,, \tag{8}$$

$$\nabla^2 \vec{B} - \frac{1}{c^2}\frac{\partial^2 \vec{B}}{\partial t^2} = -\mu_o \nabla \times \vec{J}. \tag{9}$$

Here (n_s, $\vec{u_s}$) are the number density, velocity of plasma fluid 's' (s = ions(i)/electrons(e)), ($q_{i,e} = +Z_i e, -e$), ($\vec{W}$) is the amplitudes of AGWs from (1), ν_s is the frequency of collision between species s to neutral, $\vec{B}_o$ is the Earth's magnetic field and $\vec{J}_w$ is the ionospheric current density caused by the AGWs, ($\vec{E}$, $\vec{J}$, $\vec{B}$) in the above equations are the fluctuating electric field, net current and magnetic field in the ionosphere, $\underline{\sigma}$ is the ionospheric conductivity tensor and ($c = \frac{1}{\sqrt{\mu_o \epsilon_o}}$) is the speed of light in vacuum. P, L are the production and loss of ions and electrons by photo ionization and chemical reactions. The production term 'P' in (6) is derived from SAMI2 model (Huba *et al.* 2000).The chemical loss term, 'L', in (6) is retained through effective recombination rate as taken by Kherani *et al.* (2011). In addition to the wave eq. (7), the electric field, $\vec{E}$, also satisfies the charge neutrality condition given by following equation:

$$\nabla \cdot \vec{J} = 0 \,\text{or}\, \nabla \cdot (\sigma \cdot \vec{E} + \vec{J}_w) = 0 \Rightarrow \nabla \cdot \vec{E} = -\sigma^{-1}(\vec{E} \cdot \nabla\sigma + \nabla \cdot J_w). \tag{10}$$

Eqs (2)–(10) form the closed set of equations to study the temporal and spatial variation of AGWs wind $\vec{W}$, atmospheric density/pressure (ρ, p), ionospheric number density (n), electric field $\vec{E}$ and magnetic field $\vec{B}$ anomalies. The time $t = 0$ in the simulation corresponds to the origin time (5:46:23 UT) of the tsunami. At $t = 0$, ambient atmosphere and ionosphere (p_o, ρ_o, n_o, ν, T) are obtained from SAMI2 model (Huba *et al.* 2000). The Earth's magnetic field B_o is obtained using IGRF model within the SAMI2 model. In Fig. 1, the atmospheric mass density ρ, acoustic speed $\sqrt{\gamma p/\rho}$, background zonal/meridional winds $\vec{W}_o$, kinematic viscosity ν and the ionospheric number density n_o are shown. The background winds are estimated using the HWM model that is the part of the SAMI2 model. The background wind in the stratosphere/mesosphere has decisive effects in the propagation of AGWs in the thermosphere as known from previous studies (Hickey *et al.* 2009) including our previous work (Kherani *et al.* 2011). The important effects are the filtering of high frequencies and reduction of amplitude of AGWs that reaches to the thermosphere (Hickey *et al.* 2009; Kherani *et al.* 2011). It may be noted from Fig. 1(c) that during the Tohoku-Oku tsunami, the mean wind becomes $\sim$40 m s^{-1} in the lower thermosphere that is of the same order as that of the mean wind amplitude $\sim$70–100 m s^{-1} considered by Hickey *et al.* (2009) and also by Kherani *et al.* (2011). Thus, in this work, the mean wind is expected to have appreciable effects on the propagation of AGWs as discussed later in Section 4.1. The ambient electric field is taken to be zero.

Eqs (2)–(10) are solved numerically using finite-difference method in three dimensions that is consist of altitude, latitude and longitude. The implicit Crank–Nicholson scheme is employed to perform the time integration leading to the matrix equation that is subsequently solved by the Successive-Over-Relaxation method. This methodology was adopted in our previous simulation works in two dimensions (Kherani *et al.* 2004, 2011) and three dimensions (Kherani *et al.* 2005) and is discussed in Appendix C. The magnetic dipole coordinate system (p, q, ϕ) is adopted where p, q, ϕ represent the coordinates outward normal to the Earth's magnetic field, northward directed parallel to the Earth's magnetic field and azimuth angle (+ve towards west), respectively. The N–S and E–W boundaries of simulation volume are 23°–50°N and 131°–156°E which covers the region of interest. The lower boundary for the atmosphere and ionosphere are chosen to be the ocean surface and 160 km, respectively. The upper boundary is chosen to be 600 km for both atmosphere and ionosphere.

At the lower boundary, that is, at the ocean surface–atmosphere interface, the outward normal component W_p of the wind $\vec{W}$ is continuous and is equals to W_T for all the time where W_T is the output of the tsunami model as shown in Fig. 2 and is changing with time. The tsunami wavefield, W_T, is obtained using the tsunami model with the time resolution of 1 min (Hébert *et al.* 2006). By doing so, we therefore do not have all the excitation mechanism of the atmospheric waves, as both the rupture process (the vertical induced displacement), the body waves and the Rayleigh waves are missing from this surface vertical displacement field. Our modelling will therefore be only a partial response of the quake, but is however likely to represent most of the induced gravity waves, either generated by the source uplift or by the propagating tsunami. At $t = 0$, ($W_p = W_T$) at the lower boundary and ($W_p = 0$) at other altitudes. The lower boundary condition $W_p = W_T$ at all time acts as the source for the excitation of the AGWs where other wind components W_q, W_ϕ at all time and in the whole space and W_p at all time and in the whole space except at the lower boundary are self-consistently determined from eq. (4). These perturbation winds W_p, W_q, W_ϕ of AGWs in turn cause the variations in the (p, ρ, T, n, $\vec{E}$, $\vec{B}$) from their corresponding initial values ($p = p_o$, $\rho = \rho_o$, $T = T_o$, $n = n_o$, $\vec{E} = 0$, $\vec{B} = 0$) through eqs (2)–(10). The variations in (p, ρ, T) and variations in the tsunami wavefield W_T again modify AGW and this cycle keeps repeating till $t = 80$ min when we have chosen to stop the simulation.

The boundary conditions for the wave, continuity and energy equations of AGW (2–4) and for the hydromagnetic eqs (5)–(10)

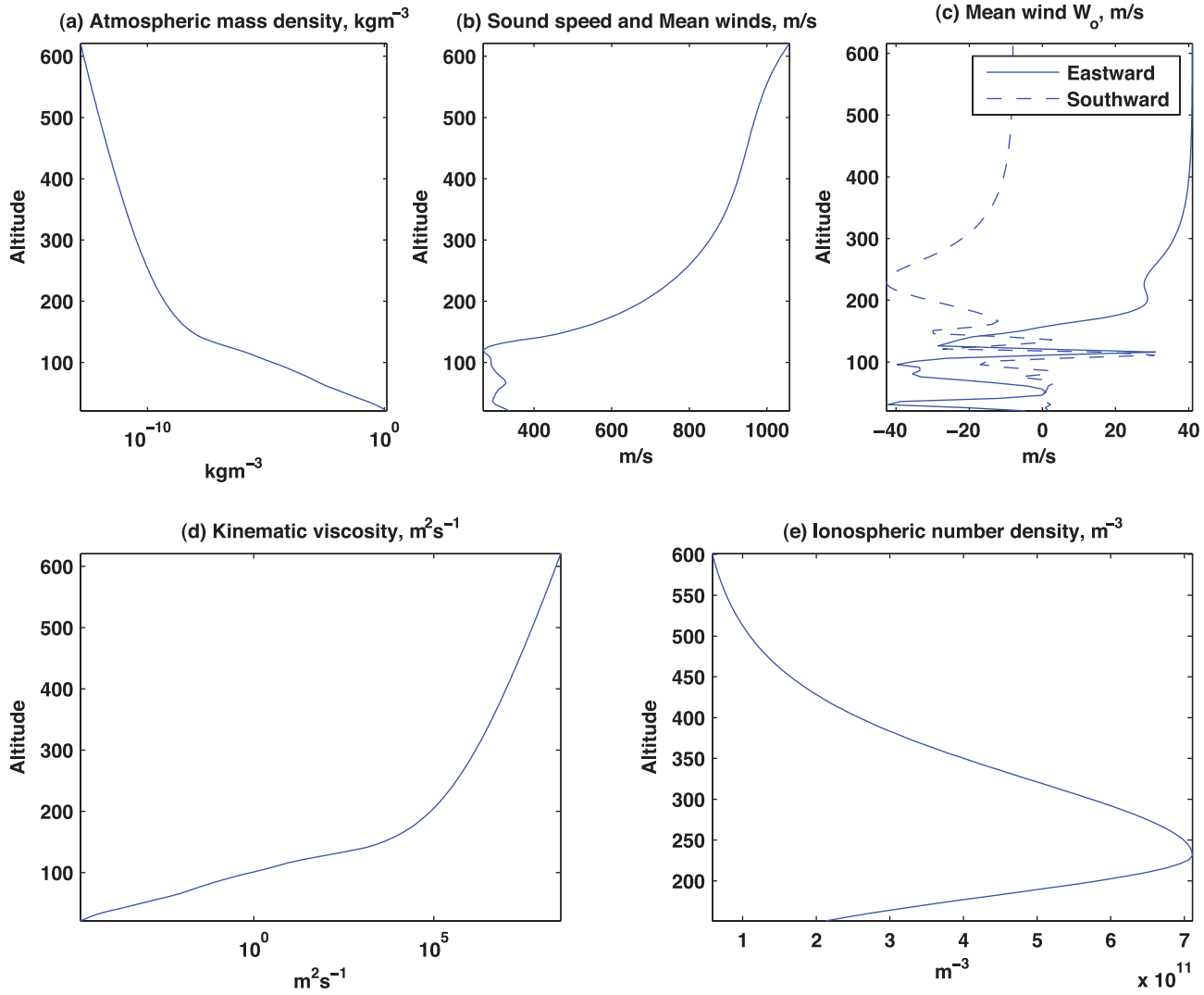

Figure 1. Initial atmosphere/ionosphere: (a) atmospheric mass density ρ, (b) acoustic speed $\sqrt{\gamma p/\rho}$, (c) the background mean wind $\vec{W}_o$, (d) kinematic viscosity ν and (e) ionospheric number density n_o.

in the ionosphere are taken to be same as taken by Kherani *et al.* (2011). As noted, the boundary condition is imposed at the lower boundary with the tsunami field for the wave eq. (4). It is conventional to use the Rayleigh friction sponge layers to damp the waves as they approach the upper boundaries, hence reducing the magnitudes of any reflected waves (Snively & Pasko 2008). However, the present model includes viscosity effects that significantly damp the waves in the thermosphere, thereby reducing artificial reflection and the influence of reflected wave energy (Snively & Pasko 2008). Thus the upper boundary is the part of the viscous absorbing layer where ν, ζ' attain the maximum value. For the ionosphere, the transmitive boundary condition (i.e gradients of the n, $\vec{J}$, $\vec{E}$, $\vec{B}$ are zero in the p direction) at lower and upper boundaries are imposed which ensures the uniform value of n, $\vec{J}$, $\vec{E}$, $\vec{B}$ at these boundaries. In other words, the ionospheric variables ($\Xi = n$, $\vec{J}$, $\vec{E}$, $\vec{B}$) satisfy following the transmitive boundary condition at 160 km and 600 km altitude:

$$\frac{\mathrm{d}\Xi}{\mathrm{d}p} = 0.$$

3 RESULTS

In Fig. 2, the snap shots of the tsunami wavefield W_T generated by the tsunami at the few selected times (between 5:46:23UT-6:46:23 UT) are shown. The origin time of tsunami is the first frame in Fig. 2 when the simulated tsunami wavefield has first finite vertical displacement and it corresponds to 5:46:23UT and will be referred as the origin time here. In Fig. 3, the vertical propagation of the simulated CADs (here referred to the p component, W_p, of the AGW) is shown at few selected times (after the origin time) in the altitude–longitude plane at fixed latitude (= 38.32°). To infer the group velocity–phase velocity relation, CADs propagation in the altitude versus time in the vicinity of the epicentre (37.6°N, 142.3°E) is plotted in Fig. 4(a). In Fig. 4(b), a similar plot is shown for the atmospheric temperature disturbance δT (defined as the difference between the instantaneous temperature and the background initial temperature). In Fig. 4(c), the time variation of the tsunami wavefield W_T in the vicinity of the epicentre (37.6°N, 142.3°E) is shown. In Figs 5–7, the simulated CADs (at 250 km altitude), temperature disturbance δT (at 250 km altitude) and CIDs are, respectively,

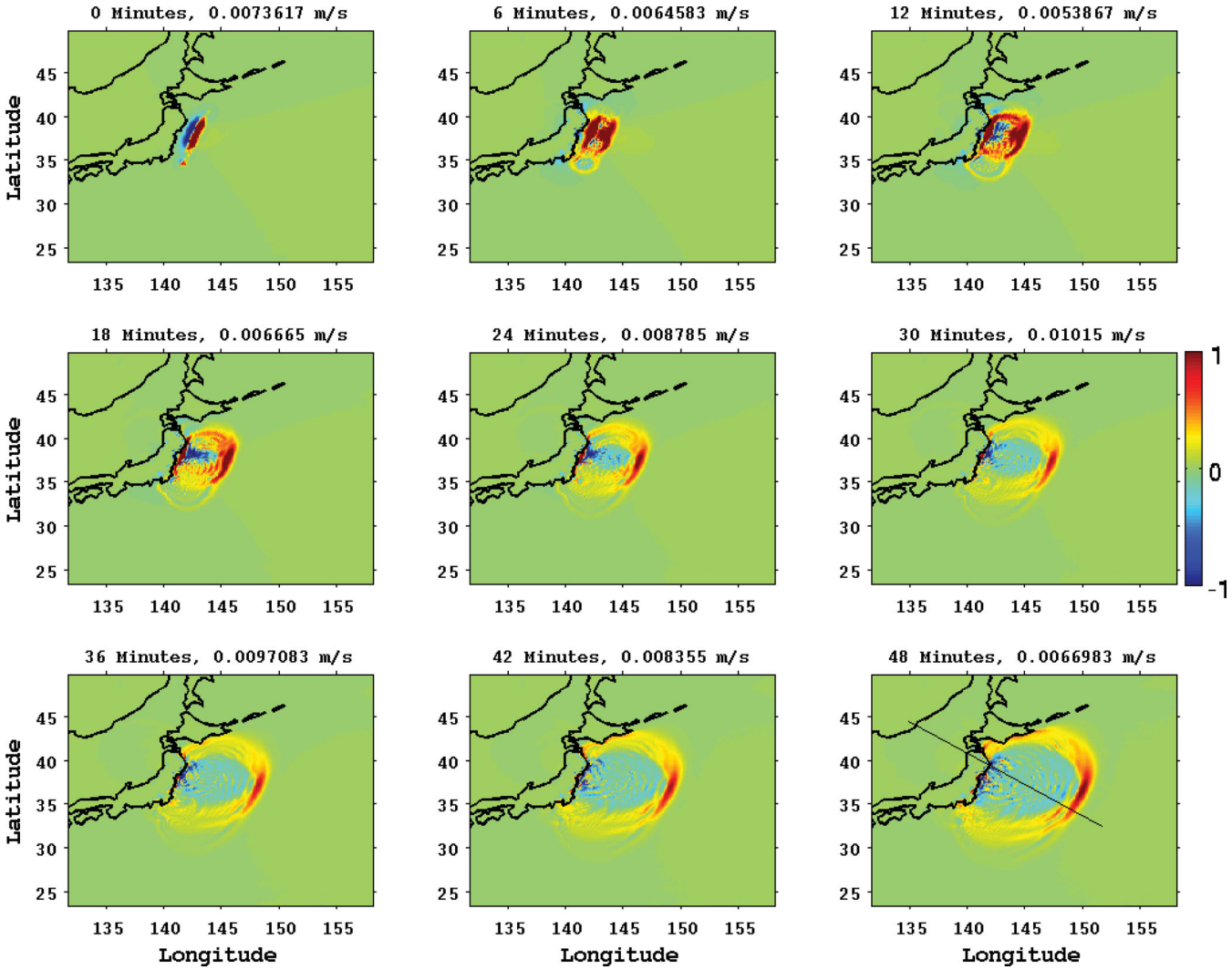

Figure 2. The tsunami wavefield W_T (normalized to the instantaneous maximum value) at few selected times after the tsunami origin time 5:46:23 UT. At the top of each panel, the time after the origin time and the maximum value of W_T is shown. The line drawn in last panel represents the horizontal cut along which traveltime diagrams in Fig. 9 are plotted.

shown at few selected times in the latitude–longitude plane, assuming only adiabatic temperature variations. Here the CIDs represents the vertically integrated total-electron-content between altitude of 160 and 450 km. In Fig. 8, GPS-measured CIDs are plotted for few selected times. These are observed Slant TEC measurements and arejust corrected into VTEC following Klobouchar (1986) approximation for a reference altitude of 250 km. A more detail study of these GPS-TEC observations is presented by Rolland *et al.* (2011b). To infer the horizontal propagating characteristics of the CADs/CIDs, the traveltime diagram (TTD) of the input tsunami wavefield, simulated CADs(at 250 km) and CIDs are plotted as a function of the distance to the epicentre versus the time after the origin time in Figs 9(a)–(c), respectively. These CADs and CIDs are obtained along the line that cuts through the horizontal plane as shown in the last panel in Fig. 2. The CADs and CIDs in these figures are low-pass filtered (periods greater than 10 min are allowed to pass) of the simulated CADs/CIDs. For comparison, the TTD of the observed CIDs from the GPS are plotted for pseudo-random noise (PRN) = 09 in Fig. 9(d). In these plots, various lines with different slopes are drawn to identify the various horizontal velocities of the wave fronts of the CADs/CIDs and GPS-CID. For the synthetic CADs/CIDs in Figs 9(b) and (c), clockwise upper and lower velocity limits are shown as solid lines and correspond to the 800 m s^{-1} and 250 m s^{-1}, respectively. In addition, two intermediate velocities are also shown as dashed lines corresponding to the 600 m s^{-1} and 300 m s^{-1}, respectively. For the GPS-CIDs, clockwise, four lines with different slopes are shown representing the velocities equal to 1 km s^{-1}, 550 m s^{-1}, 270 m s^{-1} and 170 m s^{-1}, respectively.

The vertical (Z) component of the simulated magnetic anomaly is shown in Figs 10(a) and (b). In Fig. 10(a), the simulated magnetic anomaly is plotted at 250 km altitude at time $t = 47$ min. In Fig. 10(b), the TTD of the low-pass filtered simulated component is plotted. The largest amplitude fluctuation scales to 0.5 nT in Fig. 10(b). During the Tohoku-Oki tsunami, the GSI magnetic network has provided magnetometer measurements in the vicinity of epicentre. The magnetometers registered 1 min data on several locations. To extract the tsunami-related magnetic anomaly, these data have been bandpass filtered and corrected from common mode associated to external ionospheric activity. The difference in the registered components are shown in Figs 11 and 12 and discussed in Section 4.5.

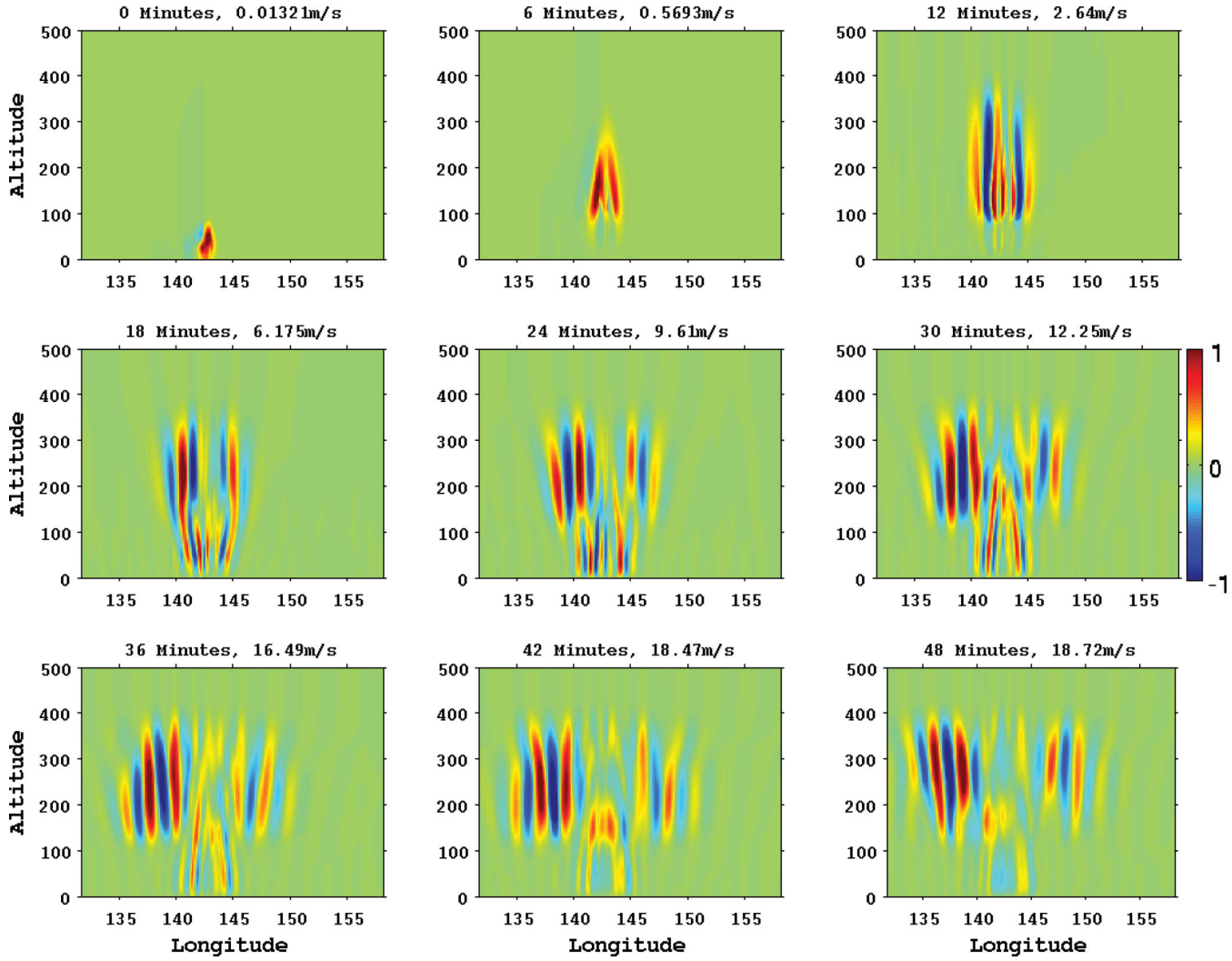

Figure 3. Vertical propagation of the simulated CADs (referred to the wind W_p component of AGWs, where W_p represents the component of the wind outward normal to the Earth's magnetic field): W_p (normalized to the instantaneous maximum value) at altitude–longitude plane at fixed latitude = 38.32° is plotted during few selected times after the tsunami origin time 5:46:23 UT. At the top of each panel, the time after the origin time and maximum value of wind amplitude is shown.

4 DISCUSSION

4.1 Vertical propagation of AGWs or CADs

The tsunami wavefield in Fig. 2 reveals the successive appearance of two tsunami wave fronts: the tsunami initial wave front (dark red/dark blue) in the vicinity of the epicentre at the beginning, that spreads away as time grows. Modelling results in Fig. 3 reveal that the initial CADs induced by the tsunami in the bottom of the atmosphere propagates upward and spreads horizontally as time progress. The CADsin the form of the longer wavelength AGW arrive to the thermospheric height (∼200 km) within 6 min that is followed by the shorter wavelength AGWs after 24 min. These two waves are likely associated with two different propagation regimes. The first one is primarily the long-wavelength AGWs (or acoustic wave), with the velocity ∼600 m s^{-1} (i.e. travelling 200 km altitude in 6 min), which is within the acoustic speed range in the thermosphere (Fig. 1b), while the second one is the short-wavelength AGWs (or gravity wave), with the smaller phase velocities ∼150 m s^{-1} (i.e. travelling 200 km altitude in 24 min) typical of the gravity waves (e.g. 250 m s^{-1} or below; Calais & Minster 1995; Ducic *et al.* 2003; Artru *et al.* 2005; Liu *et al.* 2006; Otsuka *et al.* 2006). The comparison with Fig. 2 suggests that the acoustic wave and gravity wave are caused by the primary wave front associated with the rupture and the tsunami propagation, respectively. During the tsunami/earthquake, the acoustic waves related to the rupture were first observed by Calais & Minster (1995) with the GPS-TEC technique and successfully modelled through atmospheric ray tracing (Calais *et al.* 1998; Heki & Ping, 2005; Heki *et al.* 2006; Afraimovich *et al.* 2010). During the tsunami, gravity waves associated with the tsunami propagation are observed (Artru *et al.* 2005; Rolland *et al.* 2010) and modelled using TAI coupling (Occhipinti *et al.* 2008; Hickey *et al.* 2009, 2010). In this study, the acoustic and gravity waves are simultaneously simulated that brings out additional features (as discussed in Section 4.2) in comparison to the pure acoustic or gravity wave scenario.

While propagating upwards, the amplitude of the CADs in Fig. 3 amplifies and its amplitude maximizes in 300–400 km altitude region, above which it is dissipated by the viscous processes. The CADs at the bottom of the atmosphere and at 300–400 km altitude are ∼5 × 10^{-3} m s^{-1} and ∼20 m s^{-1}, respectively. The excitation

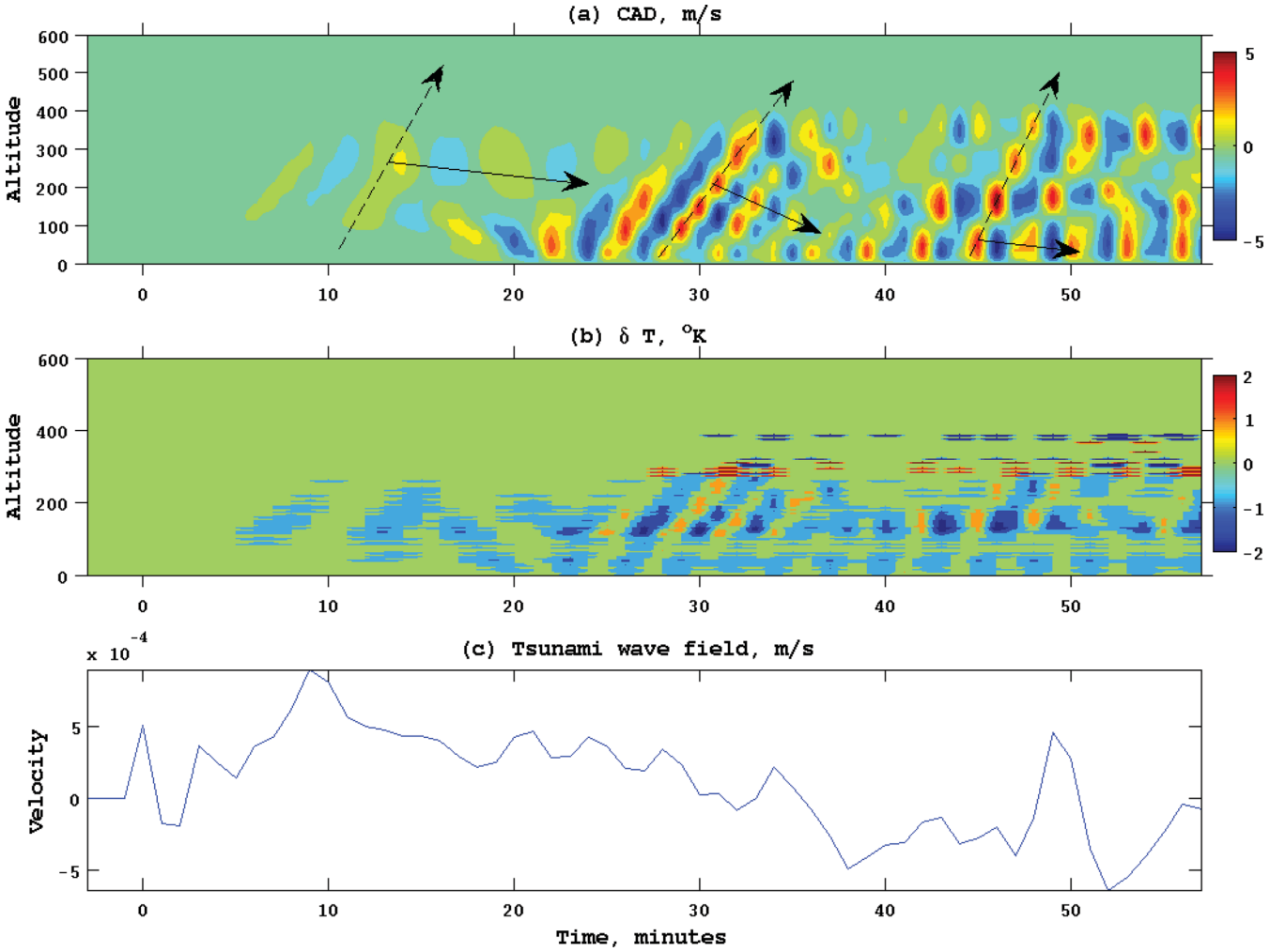

Figure 4. Group velocity–phase velocity relationship: vertical-temporal propagation of (a) CADs and (b) atmospheric temperature disturbance δT (which is the difference between the instantaneous temperature and the initial background temperature) at 37.6°N, 142.3°E (in the vicinity of the epicentre). The group and phase velocities are represented by dashed and solid lines, respectively. (c) The time-variation of the tsunami wavefield W_T at 37.6°N, 142.3°E (in the vicinity of the epicentre).

of the initial large wave followed by the short wave and amplification of the ground velocity by four orders of magnitude are known characteristics of AGWs excited by the tsunami (Artru *et al.* 2005; Occhipinti *et al.* 2006, 2008; Hickey *et al.* 2009).

It may be noted from Fig. 3 that the CADs associated with the initial impulse or uplift propagate vertical during the first 6 min and then gradually begin to spread horizontally in the thermosphere. This is in accordance with the mechanism proposed by Heki & Ping (2005) explaining that the observed TEC anomaly during the Tokachi-Oki earthquake may have been excited by coseismic uplifts of the sea surface initially as upward propagating compressive pulses of atmosphere, which were gradually refracted to propagate horizontally in the ionosphere.

From GPS-TEC measurements, Astafyeva *et al.* (2011) have reported the earlier (within 6 min) presence of CIDs related to the Tohoku-Oki tsunami and proposed the shock-acoustic wave mechanism to explain their observation. The CADs arriving to the 200 km height within 6 min in Fig. 3 is in agreement with their observation but, in the present simulation, they are associated with the acoustic wave and amplitude is too small to cause the reported CIDs ∼0.2 TECU. Thus the present simulation explains the earlier arrival of CADs/CIDs as reported by Astafyeva *et al.* (2011), but it fails to explain the large amplitude within 6 min on the basis of normal acoustic wave and may possibly need to consider the shock process. It is also possible that the small amplitude in the present simulation is owing to the nature of the tsunami wavefield (Fig. 2), which is only related to the long-period tsunami and excludes the dynamics of seismic waves (including high-frequency acoustic waves in the ocean). These seismic waves (including the acoustic waves in the ocean) will rapidly generate a much larger signal and this will be studied in future works.

A notable and novel feature in Fig. 3 is the comparatively large CADs generated when the tsunami propagates westward towards the Japan coast, as compared to the amplitude in the opposite direction, when the tsunami propagates towards the Pacific eastwards. It is however well known that the amplitude of the tsunami, and therefore the amplitude of the source of CADs, increases when the depth of the ocean decreases, as a matter of conservation of the water flow (Hébert *et al.* 2001). In Japan, this has lead to observations of tsunami height of more than 20 m on the coast, as compared to the initial amplitude of about 6 m above the epicentre (e.g. Tsushima *et al.* 2011), of which the amplitude was furthermore decreasing when the tsunami was propagating eastwards in the open Pacific Ocean. The other clear feature is the persistent westward

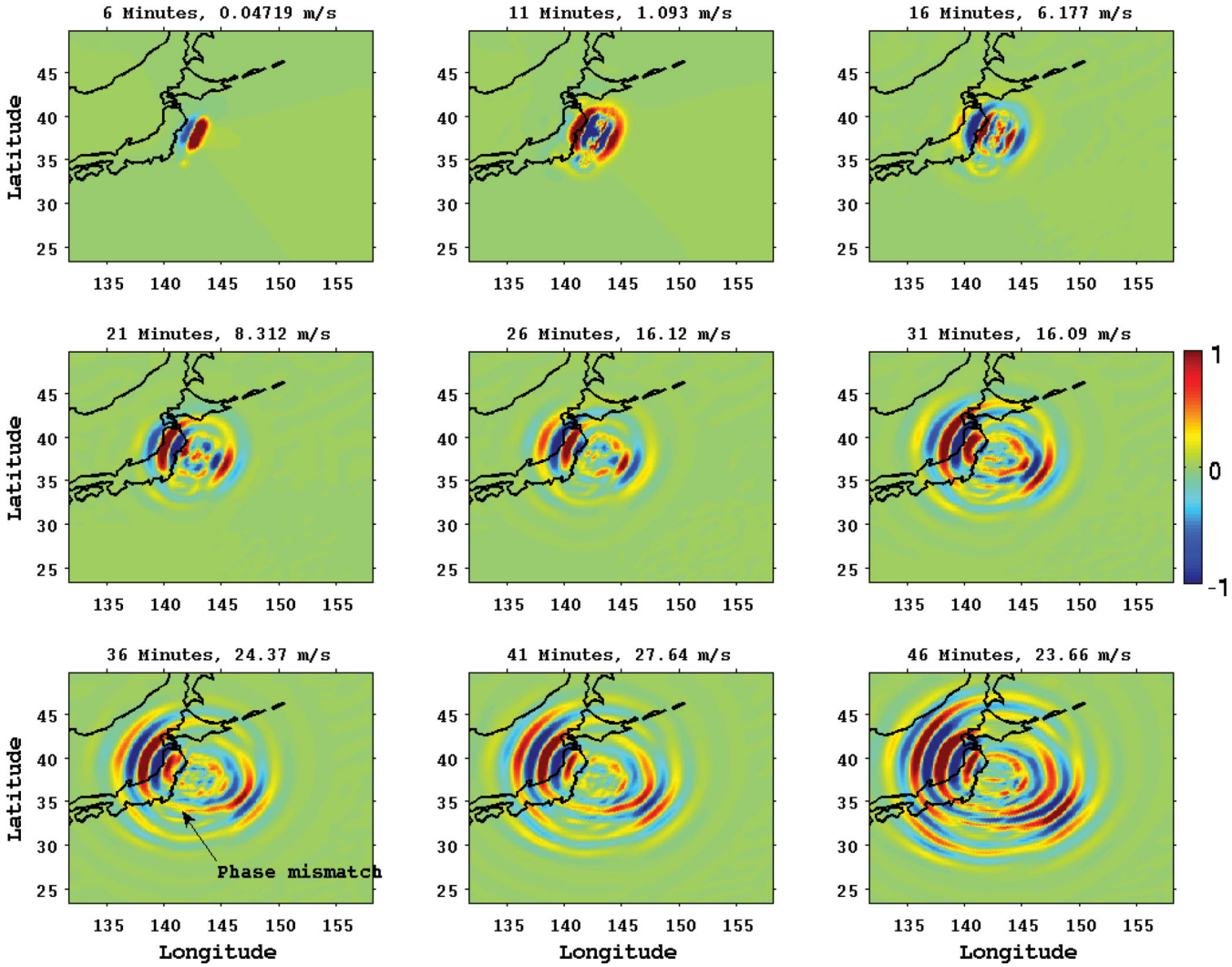

Figure 5. Spatial-Temporal characteristics of the simulated CADs or W_p: W_p (normalized to the instantaneous maximum value) at 250 km altitude is plotted during few selected time after the tsunami origin time 5:46:23 UT. At the top of each panel, the time after the origin time and maximum value of wind amplitude is shown.

propagation of CADs, even when the tsunami source has stopped due to its arrival on the coasts. Such continuous propagation was already observed in the pioneering observations of Artru *et al.* (2005), but with a much less signal-to-noise ratio.

4.2 Group velocity–phase velocity relationship

The altitude–time variation plot of CADs in Fig. 4(a) identifies the directions of the group and phase velocities as represented by the dashed and solid lines. The directions of group and phase velocities are noted to be downwards and upwards, respectively, which are consistent with the upward propagating AGWs characteristics. The atmospheric temperature disturbance δT plotted in Fig. 4(b) also reveals a similar phase and group velocities relation. This suggests that the CADs and other atmospheric anomalies simulated in this work correspond to the upward propagating AGWs. The CADs in Fig. 4(a) reflect similar evolution characteristics as noted in Fig. 3, in particular, the launching of the long-wavelength AGWs followed by the short-wavelength AGWs. From Figs 4(a) and (b), it may also be noted that the atmospheric disturbances begin to appear in the thermosphere within 6 min, suggesting the early arrival of AGWs in the thermosphere. Comparison with Fig. 4(c) suggests that with time, the frequency of AGWs or CADs changes according to the forcing tsunami wavefield. Moreover, the frequencies larger than the Brunt Väisälä frequency are excited owing to the acoustic wave dynamics and these frequencies attain large amplitude owing to the gravity wave dynamics. Such higher frequencies and early (within 6 min) arrival of AGWs or CADs in the thermosphere are not possible to be captured in the pure gravity wave scenario.

A notable feature is that the initial strong tsunami excites the weaker CADs initially in the atmosphere in comparison to the excitation of the stronger CADs by the weaker tsunami wavefield at later time. The initial large amplitude tsunami acts as a blast, launching long wavelength ∼300 km AGWs in the atmosphere as noted in Fig. 4(a). These long-wavelength AGWs does not see the mesospheric ducts whose vertical extend is ∼50 km, much smaller than the vertical long wavelength of AGWs. On the other hand, the small amplitude tsunami at later time excites the shorter

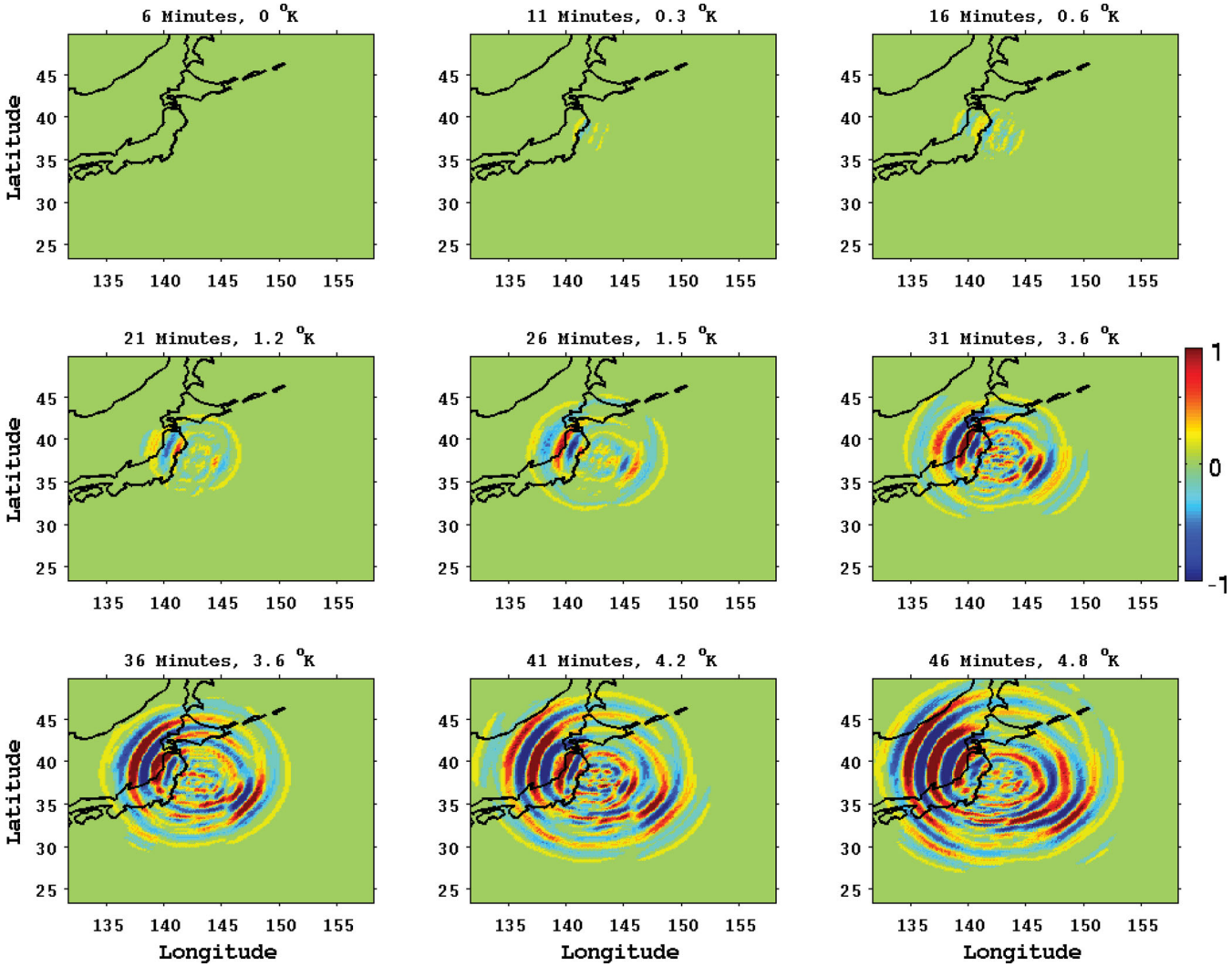

Figure 6. Spatial–temporal characteristics of the simulated atmospheric temperature disturbance δT (the difference between the instantaneous temperature and the initial background temperature): δT (normalized to the instantaneous maximum value) at 250 km altitude is plotted during few selected time after the tsunami origin time 5:46:23 UT. At the top of each panel, the time after the origin time and maximum value of temperature is shown.

wavelength ∼50–70 km AGWs as noted in Fig. 4(a) after 20 min, that are more likely to be affected by the mesospheric duct of similar vertical size, leading to the amplification of these short-wavelength AGWs within the mesospheric duct. From the mesospheric duct, the escaping of these amplified AGWs into the thermosphere is owing to the following mechanism as explained by Kherani *et al.* (2011): The amplification of $\vec{W}$ of AGWs within the duct leads to the non-linear growth of the viscous term in eq. (4), introducing large friction which resists the amplitude $\vec{W}$ of AGWs to grow within the duct. The momentary balance between non-linear viscous damping and the growth in $\vec{W}$ leads to an equilibrium which allows the AGW to escape from the duct to the thermosphere, resulting in a reduction in both $\vec{W}$ and the viscous term in eq. (4). So long forcing from the tsunami wavefield, W_T, is available, $\vec{W}$ again builds up, resulting in the growth of viscous damping term again. This leads again to the momentarily equilibrium within the duct and subsequent AGWs escaping to the thermosphere and this process continues so long as the forcing from the tsunami is available. Thus, the AGWs, that escape the mesospheric duct after going through the ducting, are greatly amplified as noted in Fig. 4(a) after 20 min.

4.3 Horizontal propagation of CADs/temperature disturbance/CIDs

Modelling results in Figs 5–7 shows that following the tsunami wavefield spatial structure, the CADs/temperature disturbance δT/CIDs appear as a dipolar-shaped anomaly increasing in the vicinity of the epicentre within 6–7 min from the origin time. At 11 min (and more profoundly at 16 min), new CADs/δT/CIDs begin to appear in the form concentric circular wave fronts in the vicinity of epicentre and start propagating radially away from the CADs/δT/CIDs origin. Later at 26 min, circular wave front remain dominant feature far away from the CADs/δT/CIDs origin, while new wave fronts, in the form of the elongated disc-shaped anomaly similar to the tsunami wavefield pattern begins to appear in the vicinity of CADs/δT/CIDs origin. These circular and elongated disc-shaped wave fronts are, respectively, associated with the acoustic wave and gravity wave as identified in Fig. 3. While these wave fronts spread in all direction, the large CADs/δT/CIDs remain focus in the backward and forward direction of the tsunami propagation. In the forward direction, they maximize across the principal wave front of the tsunami wavefield. In the backward direction, they

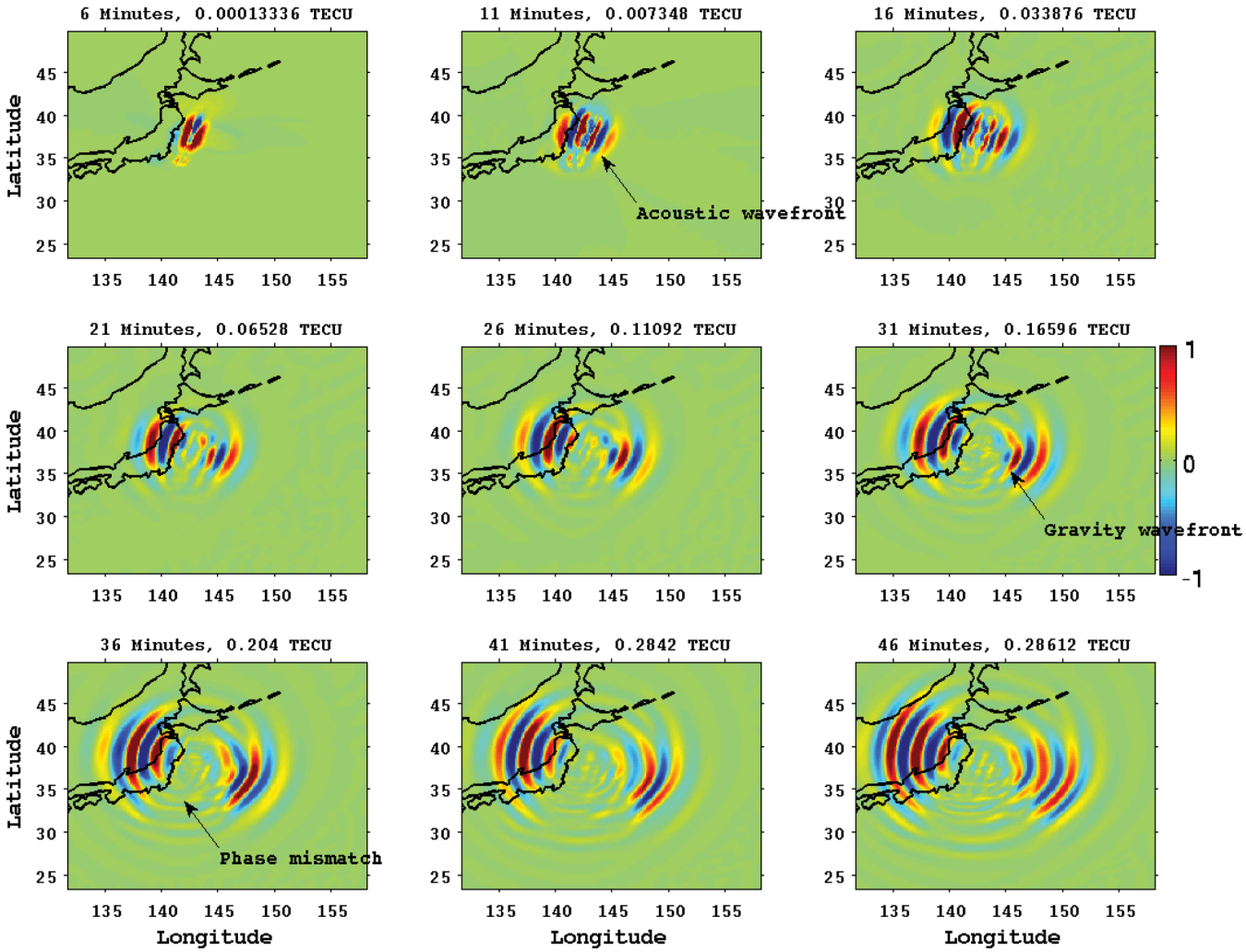

Figure 7. Spatial–temporal characteristics of the simulated CIDs or TEC: TEC disturbance (vertically integrated number density of the ionosphere from 160–450 km altitude) is plotted during few selected times after the tsunami origin time 5:46:23 UT. At the top of each panel, the time after the origin time and maximum value of TEC is shown. The plotted TEC is normalized to the instantaneous maximum value.

maximize across the region of tsunami origin. These both regions correspond to the region of large tsunami amplitude and associated horizontal gradient that lead to the excitation of strong CADs and subsequent CIDs. The wave fronts of CIDs reveal significant phase mismatching across the coast after 36 min. This phase mismatch is caused by the interference between the rapid propagating wave fronts related to acoustic waves and the slow propagating wave fronts related to the tsunami waves.

The observed CIDs in Fig. 8 reveal similar characteristics as reported by Liu *et al.* (2011), Rolland *et al.* (2011b) and Tsugawa *et al.* (2011): initial appearance of dipole-shaped CIDs in the vicinity of epicentre, followed by the radially expanding circular concentric wave fronts and lately developed elongated CIDs. Also noted is the significant phase mismatch of the wave fronts (denoted by arrow) that begin to appear across the coast at 26 min. These observed characteristics are found to be present in the synthetic CIDs in Fig. 7.

We have run the simulation without the mean wind $\vec{W}_o$ and noted that the amplitude of AGWs reduces in the presence of the mean wind and also it is dominated by longer horizontal wavelengths extending to the wider horizontal extent in the thermosphere. The reduction in the amplitude in the presence of mean wind is the known feature from the work of Hickey *et al.* (2009). The dominance of longer horizontal wavelength in the presence of mean wind is the manifestation of the presence of low-frequency AGWs in the thermosphere which otherwise will be dominated by the shorter wavelength or the high-frequency components in the absence of the mean wind. In other words, in the presence of the mean wind, the high-frequency components are filtered out which is also the known feature from the work of Kherani *et al.* (2011).

4.4 The TTDs of the CADs/CIDs

The TTD of the input tsunami wavefield in Fig. 9(a) reveals the presence of wave front moving with tsunami velocity $\sim$200 m s^{-1} (Rolland *et al.* 2010). From the TTD of the simulated CADs/CIDs as shown in Figs 9(b) and (c), the presence of the high-frequency ($\sim$10 min) acoustic wave front near the epicentre before 30 min and low-frequency ($>$10 min) gravity wave fronts far away from the epicentre after 30 min are identified (10 min is the typical Brunt-vaisala period in the thermosphere). Moreover, with time, the slope of the wave front, that is, the velocity of the CADs/CIDs gradually decreases from 800 m s^{-1} to 250 m s^{-1}. The upper limit of 800 m s^{-1} is determined by the the acoustic speed which is $\sim$800 m s^{-1}

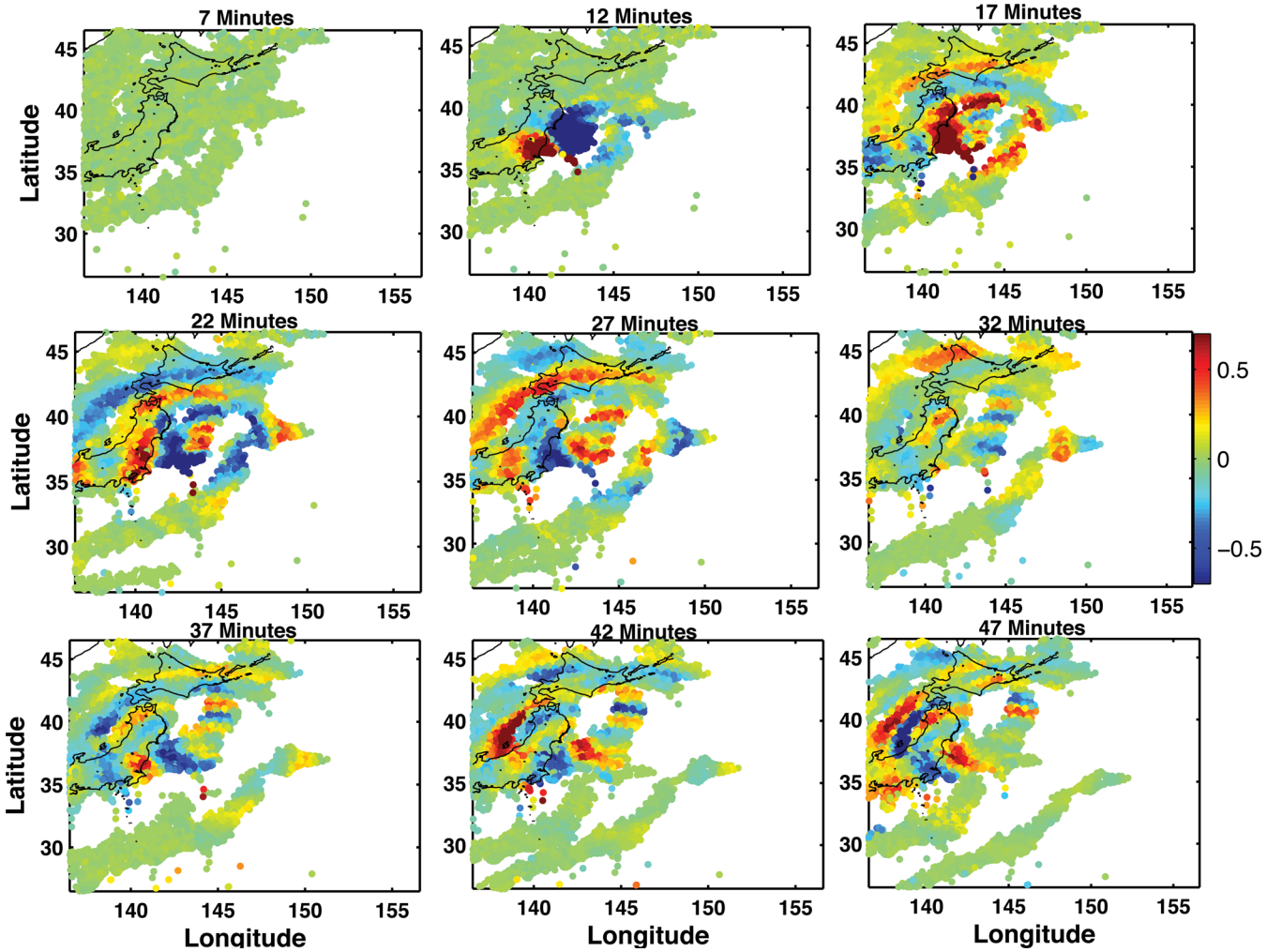

Figure 8. Observed CIDs or TEC from the GPS during few selected time similar to the Fig. 7.

at 250 km (Fig. 1b) while lower limit of 250 m s^{-1} is determined by the tsunami propagation.

The TTD of the observed CIDs as shown in Fig. 9(d) exhibits similar wave features as those reported recently by Liu *et al.* (2011), Tsugawa *et al.* (2011) and Rolland *et al.* (2011b): the CIDs moving with velocities in the wide range ∼3 km s^{-1}–220 m s^{-1} covering Rayleigh, acoustic and gravity waves. It is evident that the simulated TTDs in Figs 9(b) and (c) capture the wave fronts observed within 800–250 m s^{-1} that include the acoustic and gravity waves. Also, the transition from acoustic to gravity wave front with increasing epicentre distance and time is noted in both observed and synthetic TTDs. Few important discrepancies are also noted such as the absence of the wave fronts in the synthetic associated with the Rayleigh waves and the fast moving (∼1 km s^{-1}) acoustic waves while these wave fronts are found to be present in the observed TTDs. The observed wave fronts associated with the Rayleigh waves and moving with velocity ∼3 km s^{-1} are not modelled in this study since the tsunami model (Fig. 2) does not include these waves. The observed (1 km s^{-1}) and modelled (800 m s^{-1}) upper acoustic limit are different because the present model may not simulate the very fast wave partly owing to the ambient acoustic speed limit which is ∼800 m s^{-1} in the 200–400 km altitude region (Fig. 1b) and partly owing to the finite time–space resolution used in the simulation that limits the maximum velocity that can be resolved in the simulation.

Matsumara *et al.* (2011) have explained the observation of Tsugawa *et al.* (2011) by simulating the CADs from the impulsive source and found the presence of wave fronts moving with horizontal phase velocities in the range ∼490–220 m s^{-1} associated with the tsunami wave. In this study, the simulation is performed for CIDs as well, and both CADs/CIDs in Figs 9(b) and (c) show the presence of wave fronts with velocities in the range 800–250 m s^{-1} that cover the tsunami waves simulated by Matsumara *et al.* (2011).

Using GPS-TEC measurements, Rolland *et al.* (2011b) have also reported, for the first time, the presence of wave fronts moving with velocity ∼170 m s^{-1} originating after 1 hr from the tsunami origin. To capture this slow moving (<200 m s^{-1}) CADs/CIDs, simulation run for more than 1 hr from the origin time is desired which is not done in this study. More important are the ion-drag force and plasma diffusion that become effective in 1 hr timescale and are the efficient mechanisms to slow down the phase velocity of AGWs near the *F*-peak (Hickey *et al.* 2009). Even within 1 hr timescale, the decelerating mechanism such as heat conduction, diffusion and ion-drag may become important and may alter the propagation velocities in Figs 9(b) and (c). In this regard, it may also be noted that, in the region beyond 700 km epicentre distance, the simulated TTD is significantly different from the observed TTD, in particular, it fails to explain the observed spreading of CIDs with increasing epicentre distance. This difference is possibly caused by the omission of the

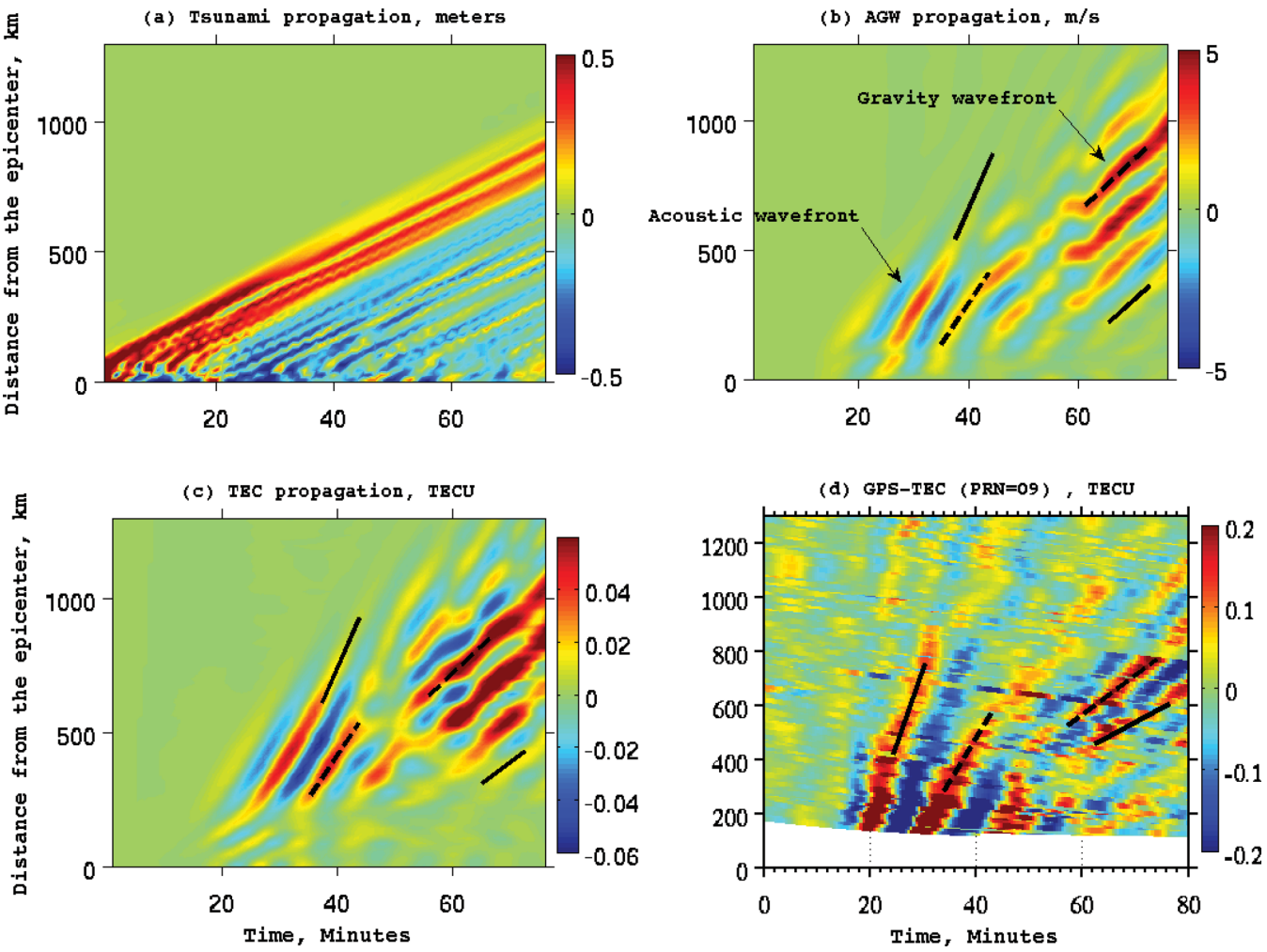

Figure 9. Traveltime diagram: the time versus epicentre distance variation (along the cut as shown in the Fig. 2) of the (a) input tsunami wavefield, (b) simulated CADs, (c) simulated CIDs and (d) observed TEC or CIDs from GPS (PRN = 09). The solid lines in (b) and (c) represent the reference lines with slopes corresponding to the upper and lower limits 800 m s^{-1}, 250 m s^{-1}, respectively. The dashed lines in (b) and (c) represent the intermediate velocities equals to the 600 m s^{-1} and 300 m s^{-1}, respectively. In (d), clockwise, four lines represent the velocities equal to the 1 km s^{-1}, 550 m s^{-1}, 270 m s^{-1} and 170 m s^{-1}, respectively.

plasma diffusion and ion drag forces. These effects are not included in this work and will be included in the future simulation work.

The comparison among modelled CIDs in Figs 7 and 9(c) and the observed CIDs in Figs 8 and 9(d) suggests that the observed features such as the timing and appearance of circular/disc-shaped wave fronts related to the acoustic and gravity/tsunami waves and the phase mismatch at later time are simulated fairly well in the present simulation. These similarities suggest that the modelling based on the TAI coupling successfully captures most of the observed wave disturbances in the CIDs.

4.5 Modelled magnetic anomaly in the F region and magnetometer measurements

From the modelled magnetic anomaly in Fig. 10(a), it may be noted that the magnetic anomaly ∼1 nT are excited in the region that covers the entire tsunami wavefield. This anomaly is found to be maximum near 300–400 km altitude region. The TTD of the simulated magnetic anomaly plotted in Fig. 10(b) reveals the presence of similar wave fronts as noted for CADs/CIDs in Figs 9(b) and (c), that is, rapidly moving/early developed wave front related to the acoustic waves and slowly moving/lately developed wave front related to the gravity/tsunami waves. Utada *et al.* (2011) have reported the tsunami-related magnetic field anomaly measured from 16 magnetometer stations, that clearly show the sharp impulsive magnetic anomaly near the epicentre and tends to broaden with distance. The time versus epicentre distance characteristics noted in the simulation in Fig. 10(b) follows the similar trend. Based on the dynamo theory, Utada *et al.* (2011) have also presented the theoretical estimation of the *Z*-component anomaly triggered by the tsunami-induced ocean current and fairly good agreement is found with the long-period measurements, with typical periods of 30 min and larger.

In the present simulation, the tsunami-induced ionospheric currents are the driving source for the simulated magnetic anomaly while the ocean currents are not considered. We therefore focus on magnetic anomalies with shorter periods.

We have used the same data set as Utada *et al.* (2011), that is, GSI magnetic data available on the GSI server (http://vldb.gsi.go.jp/sokuchi/geomag/index-e.html). Data have been processed, to subtract from all data a common Japan-wide

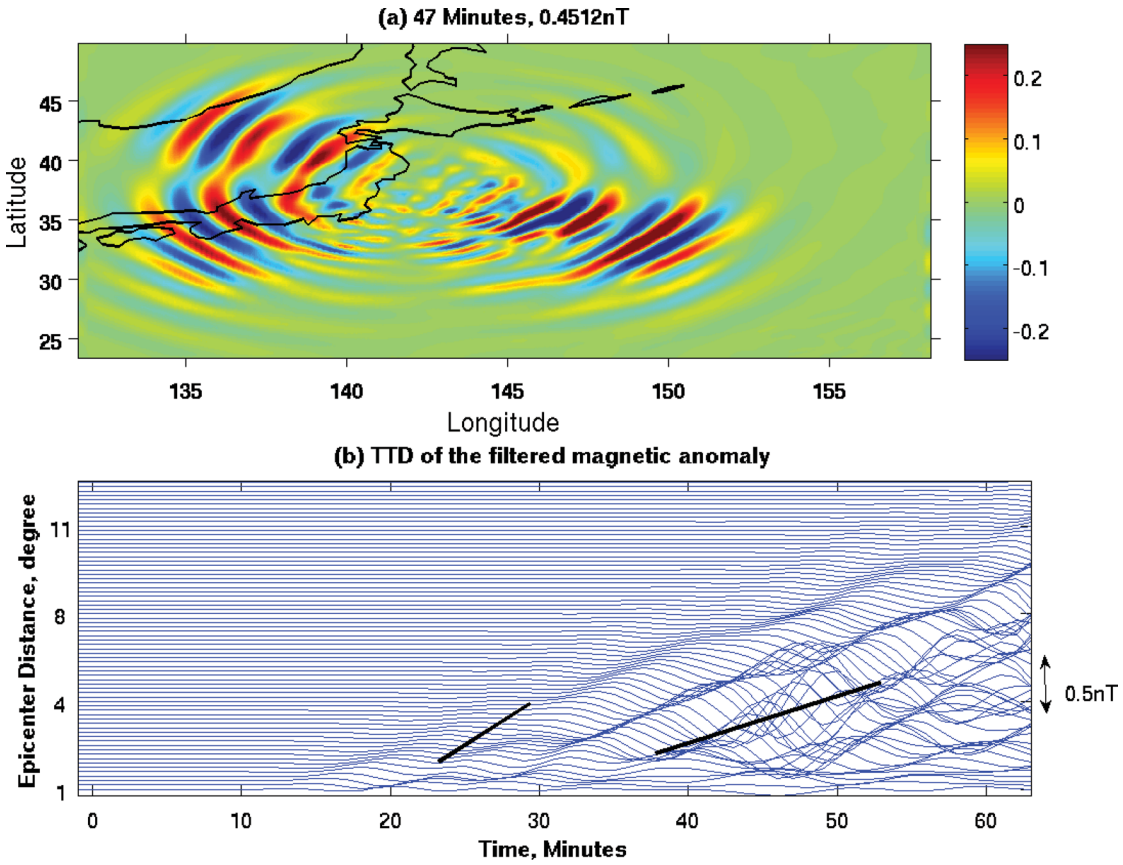

Figure 10. (a and b) Simulated vertical (Z) component magnetic anomaly $\vec{B}$ from eq. (9): (a) at 250 km altitude at 47 min with maximum amplitude indicated at the top and (b) corresponding traveltime diagram. The two continuous lines clockwise corresponding to the slopes 800 m s^{-1} and 250 m s^{-1} are also drawn.

variation, associated to the external ionospheric forcing. Such common mode is clearly seen in fig. 5 of Utada *et al.* (2011) and was obtained by computing the mean for all stations with epicentral distance larger than 5°. Additionally, data have been demeaned and detrended before filtering.

Fig. 11 shows the magnetic data on component X,Y,Z when the data are filtered in the period bandpass from 61 min to 3 min. This bandpass is performed by two simple running median. We retrieve the long-period magnetic signals, modelled by Utada *et al.* (2011). Note also that a significant part of this signal can be associated to ionospheric currents associated to either long-period TEC signals (e.g. Heki 2011) or to the long-period TEC changes which occurs after the arrival of the acoustic shock wave and are possibly associated to a ionospheric blow-off (Astafyeva *et al.* 2011). Note however that the magnetic signal is likely corrupted by seismomagnetic effects (e.g. Johnston 1997), not only for the main shock, but also for the largest aftershocks (6h15 UTC, $M_{\rm w} = 7.9$, 6h25 UTC, $M_{\rm b} = 7.1$).

A different filter, with period bandpass from 15 min to 3 min, allows to focus on the period range studied in this paper (Fig. 12). Despite the small amplitude of the ionospheric signal, this filtering allows to retrieve several magnetic features likely associated to the modelled ionospheric travelling waves. A 800 m s^{-1} wave front can be observed at distances larger than 6°, when separated to the seismo-magnetic effects, while wave trains with the lower velocities associated to the gravity waves (e.g. 200 m s^{-1}) seems also observed. We also clearly note the same large amplitudes at the same distance of 4°–5° as synthetics.

The vertical component as shown in Figs 10(a) and (b) is driven mainly by the field-align current in the F region which is the largest component in the F region owing to very large conductivity parallel to the Earth's magnetic field (Kherani *et al.* 2009). On this basis, it may be expected that the vertical Z component magnetic anomaly registered in the magnetometers may have significant contribution from the F region current, in addition to the dominant longer period contribution from the tsunami-driven ocean current, the E region current, Sq current, current in the Earth's interior and current caused by the curvature of the Earth's magnetic field. These observations and their complete interpretation will however request better modelling. Both ground, ocean, ionospheric currents are indeed expected to excite magnetic anomaly with similar trend of variation with respect to the epicentre distance as both are driven by the common quake and tsunami. The measured anomaly should integrate all these contributions. This will be the task of future works.

5 SUMMARY AND CONCLUSION

In this work, numerical simulations of the atmospheric and ionospheric anomalies are performed for the Tohoku-Oki tsunami (2011 March 11). The TAI coupling mechanism via AGWs is explored theoretically using the TAI-coupled model that involves three steps: the simulation of the realistic tsunami wavefield of Tohoku-Oki tsunami, the generation of AGWs by tsunami wavefields and the excitation of ionospheric anomalies by AGWs. For the modelled

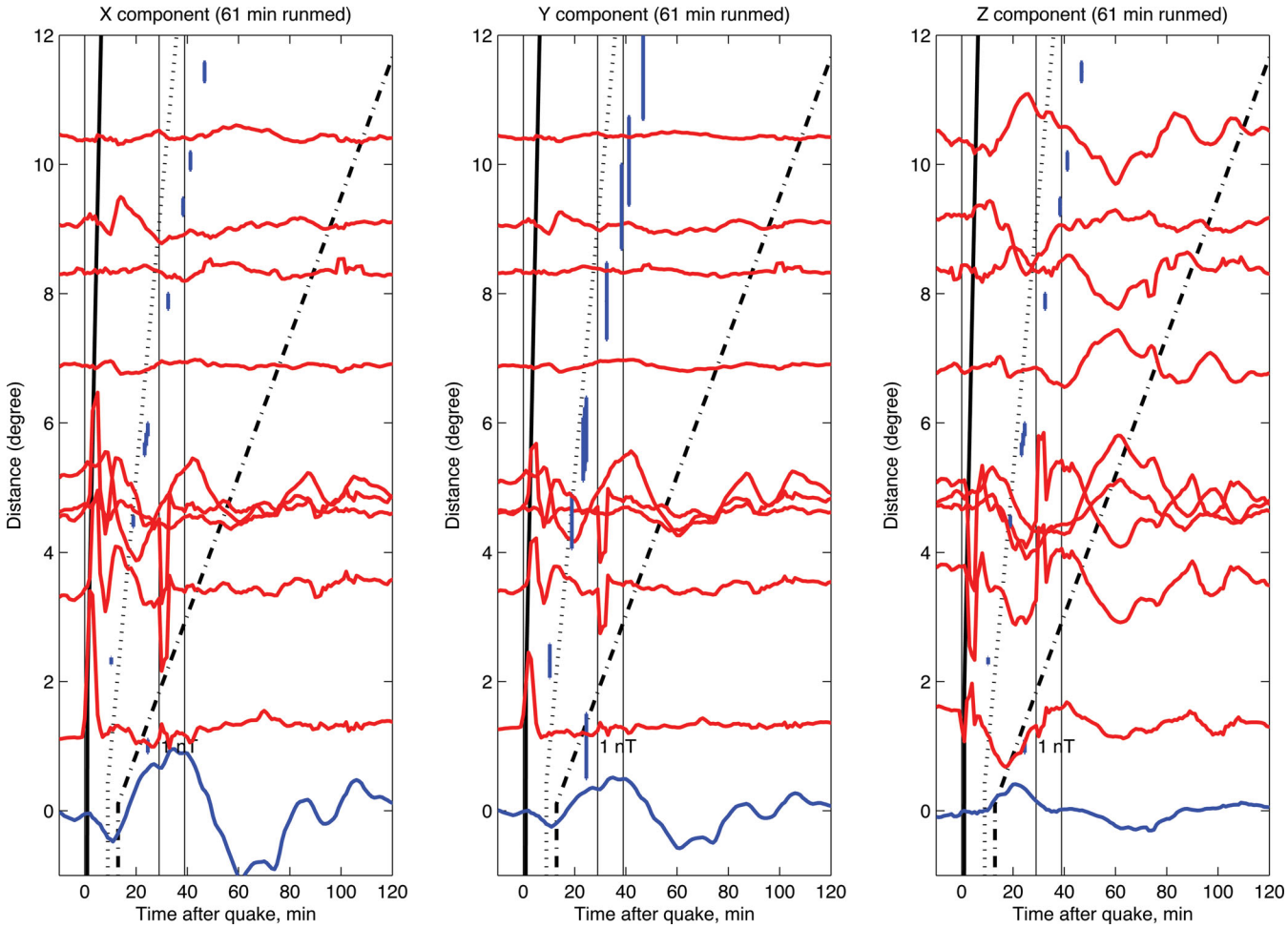

Figure 11. X,Y,Z magnetic records from GSI magnetic stations. Epicentral distance and stations are, respectively, with increasing distances in degrees and ID: 1.3 (HAR), 2.81 (YOK), 3.48 (OTA), 4.60 (SIK), 4.75 (HAG), 4.89 (AKA), 6.88 (TTK), 8.35 (MUR), 9.05 (YOS) and 10.43 (KUJ). Data have been filtered with a bandpass running median with periods of 61 min and 3 min, respectively. The bottom, blue curve is the common mode, obtained by computing the mean of all stations at distances larger than 5°. This common mode has been subtracted from all records. The scaling is increasing with distance, as the squared root of epicentre distance, to enhance 2-D propagating surface waves. The three vertical grey lines are plotted at the time of the main shock (5h46) and two major aftershocks (6h15 and 6h25). The continuous, dotted and dashed-dotted black line are for surface waves propagating at 3.6 km s^{-1} (Rayleigh waves), 800 m s^{-1} (ionospheric acoustic waves) and 250 m s^{-1} (ionospheric gravity waves), with onset 0 min, 12 min, 27 min after quake. Long-period oscillations with 15–30 min are clearly observed, as well as peaks at the arrival time of the seismic waves, likely associated to seismo-magnetic effects.

tsunami wave as an input, the coupled model simulates the wind, density and temperature anomalies in the atmosphere (or CADs) and TEC (or CIDs)/magnetic anomalies in the F region of the ionosphere. Also presented are the GPS-TEC and ground-based magnetometer measurements during the first hour of tsunami and good agreements are found between modelled and observed anomalies. The major findings in this study are summarized as follows:

(i) The simulated CADs/CIDs appear as the disc-shaped anomaly at the ionospheric height (250 km) within 6–7 min. This is followed (at 12 min from the origin time of tsunami) by the development of the concentric circular-shaped anomaly moving away from the CADs/CIDs origin. These are found to be associated with the high-frequency, long-wavelength AGWs (or acoustic wave) excited by the initial impulse or rupture. During the first 6 min, they propagate mainly vertical with the average velocity ∼600 m s^{-1} equal to the average acoustic speed in the thermosphere below 250 km altitude. After their arrival to the thermospheric height, they begin to spread horizontally with phase velocity ∼800 m s^{-1} which is the acoustic speed near 250 km altitude.

(ii) Later at 27 min, the new wave fronts, in the form of the elongated disc-shaped anomaly begin to appear in the vicinity of CADs/CIDs origin. These new wave fronts are found to be associated with the low-frequency, short-wavelength AGWs (or gravity/tsunami wave) with vertical phase velocity <200 m s^{-1} and horizontal phase velocity ∼250 m s^{-1}.

(iii) In the simulated TTD, the horizontal phase velocity of the CADs/CIDs decrease gradually from 800 m s^{-1} to 250 m s^{-1} during 10–60 min from the origin time revealing the gradual mode transfer from acoustic to gravity. However, the observed acoustic wave fronts moving at 1 km s^{-1} are not captured in the synthetic either owing to the 800 m s^{-1} ambient acoustic upper limit near 250 km altitude and/or owing to the finite space–time resolutions used in the simulation that dictates the upper velocity limit which can be resolved.

(iv) The timing and appearance of circular and elongated wave fronts, their horizontal phase velocities are found to be similar to the the GPS-TEC measurement and observed TTD presented here and also reported from recent studies.

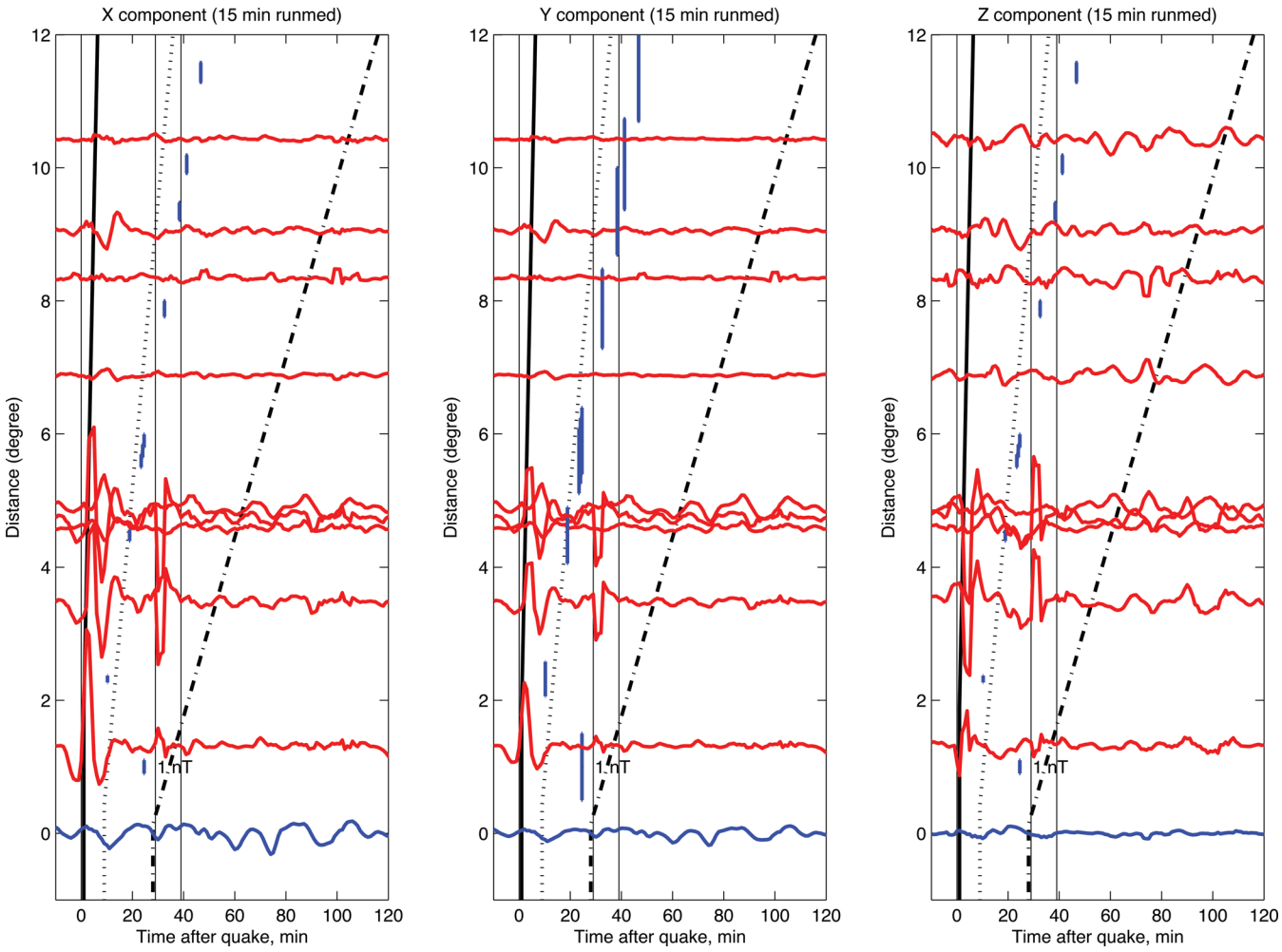

Figure 12. Same as 11, but with a bandpass between 15 min and 3 min. Travelling waves with 800 m s^{-1}, as well as dispersive ones with 250 m s^{-1} and less are observed. Note the maximum amplitudes at 4° of epicentral distances, as observed on modelling.

(v) The modelled magnetic anomaly in the F region ionosphere is found to have similar temporal variations with respect to the epicentre distance as that of the simulated CADs/CIDs.

(vi) The simulated magnetic anomaly is found to be fairly good in agreement with the magnetic anomaly registered from the ground-based magnetometers, although other magnetic signal generations mechanisms related to seismo-magnetic effects and tsunami-induced induction have to be considered for a full modelling of the magnetic signals.

(vii) CADs, CIDs and magnetic anomalies are found to maximize in the forward direction of tsunami propagation across the tsunami wave front. A novel and noteworthy feature is that they also maximize in the backward direction of propagation west of the epicentre including the region where tsunami did not travel. This is owing to the large amplitude of the tsunami and associated large horizontal inhomogeneity westward of epicentre associated to coastal tsunami height amplification which lead to the excitation of strong AGWs in the atmosphere and so CADs/CIDs.

(viii) The high-frequency (∼10 min) component of the simulated CADs/CIDs and magnetic anomalies in the F region develop within 6–7 min after the initiation of the tsunami, suggesting the importance of monitoring the high-frequency atmospheric/ionospheric anomalies for the early warning, as reported on observations (Astafyeva *et al.* 2011).

(ix) The rapid (within 6–7 min) development of the specific propagation pattern of the magnetic anomaly similar to the TEC disturbance pattern suggests that the magnetic anomaly may be an important variable for the early warning system. Given the facts that the expected tsunami signals are episodic and weak, and that the frequency/wavenumbers overlap with that of other magnetic sources, it is expected that the such pattern must also be used in any method aimed at identifying tsunami magnetic signals.

ACKNOWLEDGMENTS

EAK wishes to thank funding from FAPESP, Brazil, and IPGP, Paris, for providing research fellowship. The French side of this project was supported by CNES and by ANR project TO EOS. The results presented in this paper rely on data collected by the GSI with the GEONET GPS network and GSI magnetic observatories. We thank GSI for providing these high-quality data.

REFERENCES

Afraimovich, E.L., Feng, D., Kiryushkin, V.V., Astafyeva, E.I., Jin, S. & Sankov, V.A., 2010. TEC response to the 2008 Wenchuan earthquake in comparison with other strong earthquakes, *Int. J. Remote Sens.,* **31,** 3601–3613, doi:10.1080/01431161003727747.

Artru, J., Farges, T. & Lognonné, P., 2004. Acoustic waves generated from seismic surface waves: propagation properties determined from Doppler sounding observations and normal mode modeling, *Geophys. J. Int.,* **158,** 1067–1077, doi:10.1111/j.1365-246X.2004.02377.x.

Artru, J., Ducic, V., Kanamori, H., Lognonné, P. & Murakami, M., 2005. Ionospheric detection of gravity waves induced by tsunamis, *Geophys. J. Int.,* **160,** 840–848, doi:10.1111/j.1365-246X.2005.02552.x.

Astafyeva, E., Lognonné, P. & Rolland, L., 2011. First ionosphere images for the seismic slip of the Tohoku-oki earthquake, *Geophys. Res. Lett.,* **38,** doi:10.1029/2011GL049623.

Calais, E. & Minster, J.B., 1995. GPS detection of ionospheric perturbations following the January 17, 1994, Northridge earthquake, *Geophys. Res. Lett.,* **22,** 1045–1048, doi:10.1029/95GL00168.

Calais, E., Minster, J.B., Hofton, M. & Hedlin, M., 1998. Ionospheric signature of surface mine blasts from GPS measurements, *Geophys. J. Int.,* **132,** 191–202.

Chen, C.H. *et al.*, 2011. Long-distance propagation of ionospheric disturbance generated by the 2011 Tohoku Earthquake, *Earth Planets Space,* **63,** 881–884, doi:10.5047/eps.2011.06.026.

Dautermann, T., Calais, E., Lognonné, P. & Mattioli, G.S., 2009. Lithosphere-atmosphere-ionosphere coupling after the 2003 explosive eruption of the Soufriere Hills Volcano, Montserrat, *Geophys. J. Int.,* **179,** 1537–1546, doi:10.1111/j.1365-246X.2009.04390.x.

Ducic, V., Artru, J. & Lognonné, P., 1951. Ionospheric remote sensing of the Denali Earthquake Rayleigh surface waves, *Geophys. Res. Lett.,* **30,** doi: 10.1029/2003GL017812

de Groot-Hedlin, C., Hedlin, M.A.H. & Walker, K., 2011. Finite difference synthesis of infrasound propagation through a windy, viscous atmosphere: application to a bolide explosion detected by seismic networks, *Geophys. J. Int.,* **185,** 305–320, doi: 10.1111/j.1365-246X.2010.04925.x.

Heki, K., 2011. Ionospheric electron enhancement preceding the 2011 Tohoku-Oki earthquake, *Geophys. Res. Lett.,* **38,** L17312, doi:1029/2011GL047908.

Heki, K. & Ping, J., 2005. Directivity and apparent velocity of the coseismic ionospheric disturbances observed with a dense GPS array, *Earth planet. Sci. Lett.,* **236,** 845–855, doi:10.1016/j.epsl.2005.06.010.

Heki, K., Otsuka, Y., Choosakul, N., Hemmakorn, N., Komolmis, T. & Maruyama, T., 2006. Detection of ruptures of Andaman fault segments in the 2004 great Sumatra earthquake with coseismic ionospheric disturbances, *J. geophys. Res.,* **111,** B09313, doi:10.1029/2005JB004202.

Hébert, H., Heinrich, P., Schindel, F. & Piatanesi, A., 2001. Far-field simulation of tsunami propagation in the Pacific Ocean' impact on the Marquesas Islands (French Polynesia), *J. geophys. Res.,* **106,** 9161–9177.

Hébert, H., Sladen, A. & Schindel, F., 2006. Numerical modeling of the great 2004 Indian Ocean tsunami: focus on the Mascarene Islands, *Bull. Seismol. Soc. Am.,* **97**(1A), S208–S222.

Hickey, M.P., Schubert, G. & Walterscheid, R.L., 2009. Propagation of tsunami driven gravity waves into the thermosphere and ionosphere, *J. geophys. Res.,* **114,** A08304, doi:10.1029/2009JA014105.

Hickey, M.P., Schubert, G. & Walterscheid, R.L., 2010. Atmospheric airglow fluctuations due to a tsunami-driven gravity wave disturbance, *J. geophys. Res.,* **115,** A06308, doi:10.1029/2009JA014977.

Huba, J., Joyce, G. & Fedder, J., 2000. SAMI2 is another model of the ionosphere (SAMI2): a new low latitude ionosphere model, *J. geophys. Res.,* **105**(A10), 23 035–23 053.

Johnston, M.J.S., 1997. Review of electric and magnetic fields accompanying seismic and volcanic activity, *Surv. Geophys.,* **18,** 441–476.

Kherani, E.A., de Paula, E.R. & Bertoni, F.C.P., 2004. Effects of the fringe field of Rayleigh-Taylor instability in the equatorial E and valley regions, *J. geophys. Res.,* **109,** A12310, doi:10.1029/2003JA010364.

Kherani, E.A., Mascarenhas, M., Sobral, J.H.A., de Paula, E.R. & Bertoni, F.C., 2005, A three dimension simulation model of collisional interchange instability, *Space Sci. Rev.,* **121,** 253–269.

Kherani, E.A., Lognonné, P., Kamath, N., Crespon, F. & Garcia, R., 2009. Response of the ionosphere to the seismic triggered acoustic waves: electron density and electromagnetic fluctuations, *Geophys J. Int.,* **176,** 1–13, doi:10.1111/j.1365-246X.2008.03818.x.

Kherani, E.A., Abdu, M.A., Fritts, D. & de Paula, E.R., 2011. The acoustic gravity wave induced disturbances in the equatorial Ionosphere, in *Aeronomy of the Earth's Atmosphere and Ionosphere,* eds Abdu, M.A., Pancheva D. & Bhattacharyya, A., Springer IAGA Spacial Soporan Book Series, the Netherlands.

Klobuchar, J.A., 1986. Ionospheric time-delay algorithm for single frequency GPS users, *IEEE Trans. Aerosp. Electron. Syst.,* **23**(3), 325–D331.

Landau, L.D. & Lifshits, E.M., 1987. *Fluid Mechanics, Volume 6 of Course of Theoretical Physics,* Butterworth-Heinemann, Oxford.

Liu, J.Y., Chen, C.H., Lin, C., Tsai, H.F., Chen, C.H. & Kamogawa, M., 2011. Ionospheric disturbances triggered by the 11 March 2011 M9.0 Tohoku earthquake, *J. geophys. Res.,* **116,** A06319, doi:10.1029/2011JA016761.

Liu, J.Y. *et al.*, 2006. Ionospheric GPS total electron content (TEC) disturbancies triggered by the 26 December 2004 Indian Ocean tsunami, *Geophys. Res.,* **111,** A05303, doi:10.1029/2005JA011200.

Lognonné, P., 2009. Seismic waves from atmospheric sources and atmospheric/ionospheric signatures of seismic waves, in *Infrasound Monitoring for Atmospheric Studies,* pp. 281–304, eds Le Pichon, A., Blanc, E. & Hauchecorne, A., Springer, Dordrecht.

Lognonné, P., Clévédé, C. & Kanamori, H., 1998. Normal mode summation of seismograms and barograms in an spherical Earth with realistic atmosphere, *Geophys. J. Int.,* **135,** 388–406, doi:10.1046/j.1365-246X.1998.00665.x.

Lognonné, P. *et al.*, 2006. Ground based GPS tomography of ionospheric post-seismic signal, *Planet. Space Sci.,* **54,** 528–540, doi:10.1016/j.pss.2005.10.021.

Maeda, T., Furumura, T., Sakai, S. & Shinohara, M., 2011. Significant tsunami observed at ocean-bottom pressure gauges during the 2011 off the Pacific coast of Tohoku Earthquake, *Earth Planets Space,* **63,** 803–808.

Makela, J.J. *et al.*, 2011. Imaging and modeling the ionospheric airglow response over Hawaii to the tsunami generated by the Tohoku earthquake of 11 March 2011, *Geophys. Res. Lett.,* **38,** L00G02, doi:10.1029/2011GL047860.

Maruyama, T., Tsugawa, T., Kato, H., Saito, A., Otsuka, Y. & Nishioka, M., 2011. Ionospheric multiple stratifications and irregularities induced by the 2011 Tohoku earthquake, *Earth Planets Space,* **63,** 869–873.

Matsumura, M., Saito, A., Iyemori, T., Shinagawa, H., Tsugawa, T., Otsuka, Y., Nishioka, M. & Chen, C.H., 2011. Numerical simulations of atmospheric waves excited by the 2011 off the Pacific coast of Tohoku Earthquake, *Earth Planets Space,* **63,** 885–889, doi:10.5047/eps.2011.07.015.

Nishimura, T., Munekane, H. & Yarai, H., 2011. The 2011 off the Pacific coast of Tohoku Earthquake and its aftershocks observed by GEONET, *Earth Planets Space,* **63,** 631–636.

Occhipinti, G., Lognonné, P., Kherani, E.A. & Hébert, H., 2006. Three-dimensional waveform modeling of ionospheric signature induced by the 2004 Sumatra tsunami, *Geophys. Res. Lett.,* **33,** L20104, doi:10.1029/2006GL026865.

Occhipinti, G., Kherani, E.A. & Lognonné, P., 2008. Geomagnetic dependence of ionospheric disturbances induced by tsunamigenic internal gravity waves, *Geophys. J. Int.,* **173,** 753–755, doi:10.1111/j.1365-246X.2008.03760.x.

Occhipinti, G., Coisson, P., Makela, J.J., Allgeyer, S., Kherani, E.A., Hébert, H. & Lognonné, P., 2011. Three-dimensional numerical modeling of tsunami-related internal gravity waves in the Hawaiian atmosphere, *Earth Planets Space,* **63,** 847–851, doi:10.5047/eps.2011.06.051.

Otsuka, Y., *et al.*, 2006. GPS detection of total electron content variations over Indonesia and Thailand following the 26 December 2004 earthquake, *Earth Planets Space,* **58,** 159–165.

Pitteway, M.L.V. & Hines, C.O., 1963. The viscous damping of atmospheric gravity waves, *Can. J. Phys.,* **41,** 1935–1948.

Rolland, L.M., Occhipinti, G., Lognonné, P. & Loevenbruck, A., 2010. Ionospheric gravity waves detected offshore Hawaii after tsunamis, *Geophys. Res. Lett.,* **37,** L17101, doi:10.1029/2010GL044479.

Rolland, L.M., Lognonné, P. & Munekane, H., 2011a. Detection and modeling of Rayleigh wave induced patterns in the ionosphere, *J. geophys. Res.,* **116,** A05320, doi:10.1029/2010JA016060.

Rolland, L.M., Lognonné, P., Astafyeva, E., Kherani, E.A., Kobayashi, N., Mann, M. & Munekane, H., 2011b. The resonant response of the ionosphere imaged after the 2011 Tohoku-Oki earthquake, *Earth Planets Space,* **63,** 853–857, doi:10.5047/eps.2011.06.020.

Snively, J.B. & Pasko, V.P., 2008, Excitation of ducted gravity waves in the lower thermosphere by tropospheric sources, *J. geophys. Res.,* **113,** A06303, doi:10.1029/2007JA012693.

Tsugawa, T., Saito, A., Otsuka, Y., Nishioka, M., Maruyama, T., Kato, H., Nagatsuma, T. & Murata, K.T., 2011. Ionospheric disturbances detected by GPS total electron content observation after the 2011 Tohoku Earthquake, *Earth Planets Space,* **63,** 875–879, doi:10.5047/eps.2011.06.035.

Tsushima, H. *et al.*, 2011. Near-field tsunami forecasting using offshore tsunami data from the 2011 off the Pacific coast of Tohoku Earthquake, *Earth Planets Space,* **63,** 821–826.

Utada, H. *et al.*, 2011. Geomagnetic field changes in response to the 2011 off the Pacific Coast of Tohoku Earthquake and Tsunami, *Earth planet. Sci. Lett.,* **311,** 11–27, doi:10.1016/j.epsl.2011.09.036.

APPENDIX A: DERIVATION OF THE DISPERSION RELATION FROM THE WAVE EQUATION OF AGW WITHOUT DISSIPATION

At the first step, we derive the dispersion relation of AGW using the first four terms of the wave eq. (4), that is, for the non-dissipative AGWs:

$$\frac{\partial^2 \vec{W}}{\partial t^2} = \frac{\gamma p}{\rho}\nabla\big(\nabla\cdot\vec{W}\big) + (\gamma-1)\frac{\nabla p}{\rho}\nabla\cdot\vec{W} - \frac{\nabla p}{\rho}\big(\vec{W}\cdot\nabla\big)\log\rho + \frac{1}{\rho}\nabla\big(\vec{W}.\nabla\big)p. \tag{A1}$$

Adopting the Cartesian coordinate such that $\hat{z}$ and $\hat{x}$ represent the unit vectors in the vertical and horizontal directions, following coupled scalar equations are obtained:

$$\frac{\partial^2 W_z}{\partial t^2} = c^2\frac{\partial}{\partial z}\big(\nabla\cdot W\big) + (\gamma-1)\zeta\nabla\cdot\vec{W} + \zeta\frac{\partial W_z}{\partial z} + W_z\frac{\partial\zeta}{\partial z};\quad \zeta = \frac{1}{\rho}\frac{\partial p}{\partial z}; \tag{A2}$$

and

$$\frac{\partial^2 W_x}{\partial t^2} = c^2\frac{\partial}{\partial x}\big(\nabla\cdot W\big) + \zeta\frac{\partial W_z}{\partial x}. \tag{A3}$$

Considering the plane-wave solution of the following form:

$$(W_z, W_x) \equiv (W_z^o, W_x^o)\mathrm{e}^{[\mathrm{i}(k_x x + k_z z - \omega t) + z/2H]}$$

lead to the following algebraic equations for W_z, W_x:

$$\left(-\omega^2 + k_z^2c^2 + \frac{c^2}{4H^2} - \mathrm{i}\gamma\zeta k_z\right)W_z + (k_z k_x c^2 - \mathrm{i}(\gamma-1)\zeta k_x)W_x = 0, \tag{A4}$$

$$(k_z k_x c^2 - \mathrm{i}\zeta k_x)W_z + (-\omega^2 + k_x^2c^2)W_x = 0, \tag{A5}$$

where ω, k_z, k_x are the frequency, vertical wavenumber and horizontal wavenumber, respectively, of the normal modes. The real part of condition of non-trivial solution of above coupled algebraic equations lead to the following dispersion relation:

$$\omega^4 - \omega^2c^2\left(k^2 + \frac{1}{4H^2}\right) + (\gamma-1)\zeta^2k_x^2 = 0 \tag{A6}$$

or

$$-\frac{\omega^4}{c^2} + \omega^2\left(k^2 + \frac{1}{4H^2}\right) = N^2k_x^2;\quad N^2 = (\gamma-1)\frac{\zeta^2}{c^2} \equiv (\gamma-1)\frac{c^2}{\gamma^2H^2}. \tag{A7}$$

(A7) is the dispersion relation of non-dissipative AGWs in the atmosphere (Hickey *et al.* 2009).

APPENDIX B: DERIVATION OF THE DISPERSION RELATION FROM THE WAVE EQUATION OF AGW WITH DISSIPATION

The next step is to introduce the viscous term in eq. (A1) (here only first viscous term from eq. (4) is considered), that is,

$$\frac{\partial^2 \vec{W}}{\partial t^2} = \frac{\gamma p}{\rho}\nabla\big(\nabla\cdot\vec{W}\big) + (\gamma-1)\frac{\nabla p}{\rho}\nabla\cdot\vec{W} - \frac{\nabla p}{\rho}\big(\vec{W}\cdot\nabla\big)\log\rho + \frac{1}{\rho}\nabla\big(\vec{W}\cdot\nabla\big)p + \frac{\partial}{\partial t}\left(\nu\nabla^2\vec{W}\right).$$

With the dissipative term, eqs (A4) and (A5) are modified as follows:

$$(-\omega^2 + \mathrm{i}\omega\nu\left(k^2 + \frac{1}{4H^2}\right) + k_z^2c^2 + \frac{c^2}{4H^2} - \mathrm{i}\gamma\zeta k_z)W_z + (k_z k_x c^2 - \mathrm{i}(\gamma-1)\zeta k_x)W_x = 0 \tag{B1}$$

$$(k_z k_x c^2 - \mathrm{i}\zeta k_x)W_z + (-\omega^2 + \mathrm{i}\omega\nu\left(k^2 + \frac{1}{4H^2}\right) + k_x^2 c^2)W_x = 0 \tag{B2}$$

These coupled algebraic equations lead to following dispersion relation:

$$-\frac{\omega^2}{c^2}(\omega+\eta)^2 + \omega(\omega+\eta)\left(k^2 + \frac{1}{4H^2}\right) = N^2 k_x^2; \tag{B3}$$

where

$$\eta = \mathrm{i}\nu(k^2 - \frac{1}{4H^2} - \mathrm{i}k_z/H); \quad \nu = \frac{\mu}{\rho}.$$

(B3) represents the dispersion relation of dissipative AGW and is similar to the dispersion relation derived by Pitteway & Hines (1963).

APPENDIX C: NUMERICAL METHOD

Eqs (2)–(10) are solved using centred-space finite-difference method. For the first- and second-order time derivatives, the forward and centred schemes are adopted, respectively, as follows:

$$\frac{\partial n}{\partial t} \equiv \frac{n(t+\Delta t) - n(t)}{\Delta t}; \quad \frac{\partial^2 W}{\partial t^2} \equiv \frac{W(t+\Delta t) - 2W(t) + W(t-\Delta t)}{\Delta t^2}. \tag{C1}$$

For the time integration of eqs (2)–(9), Cranck–Nicholson implicit scheme is used so that terms other than the time derivative term are estimated at $t + \Delta t$. For example, the wave eq. (4) is written as follows:

$$\frac{W'(t+\Delta t) - 2W'(t) + W'(t-\Delta t)}{\Delta t^2} = f(t+\Delta t), \tag{C2}$$

where

$$f = \frac{1}{\rho}\nabla\left(\gamma p \nabla\cdot\vec{W}'\right) - \frac{\nabla p}{\rho}\nabla\cdot\left(\rho\vec{W}'\right) + \frac{1}{\rho}\nabla\left(\vec{W}'\cdot\nabla\right)p + \frac{\partial}{\partial t}\left(\nu\nabla^2\vec{W}' + \left(\zeta' + \frac{\nu}{3}\right)\nabla(\nabla\cdot\vec{W}')\right) - \frac{\partial}{\partial t}\left(\vec{W}'.\nabla\vec{W}'\right),$$

that is, f is estimated at time $t + \Delta t$. (C2) can be rearranged as follows:

$$\begin{aligned} W'(\vec{r}, t+\Delta t) = {} & A_{\pm}W'(\vec{r}\pm\Delta r, t+\Delta t) + B_{\pm}W'(\vec{r}\pm\Delta r, t) + C_{\pm}W'(\vec{r}\pm\Delta r, t-\Delta t) + DW'(\vec{r}, t) \\ & + EW'(\vec{r}, t-\Delta t) + F. \end{aligned} \tag{C3}$$

Here coefficients A, B, C, D, E, F are the functions of $\rho(t+\Delta t)$, $p(t+\Delta t)$ which are the simultaneous solutions of eqs (2) and (3). Eq. (C3) leads to the set of algebraic equations for $W'(\vec{r}, t+\Delta t)$ where each equation is obtained by changing the grid point $\vec{r}$. Since, in the three dimension as in the present case, the number of grid points are large, (C3) represents the matrix equation with the large coefficient matrix. This matrix equation is solved using the Successive-Over-relaxation (SOR) method.